INSIGHT IN THE THIN-FILM POLLYAMIDE MEMBRANE STRUCTURE AFTER COMPACTION

Jasna Blazheska

Jasna Blazheska

Insight in the thin-film polyamide membrane structure after compaction

Doctoral Thesis

Supervised by Prof. Dr. Ricard Garcia-Valls

Co-supervised by Dr. Verónica Gómez Cortés

Co-supervised by Dr. Derek M. Stevens

Department of Chemical Engineering

Universitat Rovira i Virgili

UNIVERSITAT
ROVIRA i VIRGILI

Tarragona

2016

UNIVERSITAT ROVIRA i VIRGILI

Departament d'Enginyeria Química
Av. Països Catalans, 26
43007 Tarragona
Tel. +34 977 559 603
Fax. +34 977 559 621

I, Prof. Dr. Ricard Garcia-Valls, professor in Universitat Rovira i Virgili (URV), member of the Escola Tècnica Superior d'Enginyeria Química (ETSEQ), member of Centre tecnològic de la Química de Catalunya (CTQC),

I, Dr. Verónica Gómez Cortés, Tarragona R&D Leader by the Dow Chemical Company

I, Dr. Derek M. Stevens, Associate Scientist by the Dow Chemical Company

CERTIFY:

That the present work entitled "Insight in the thin-film polyamide membrane structure after compaction", presented by Jasna Blazheska to obtain the degree of doctor by the Universitat Rovira i Virgili, has been carried out under my supervision at the Chemical Engineering Department.

Tarragona, 29th August 2016

Prof. Dr. Ricard Garcia-Valls

Dr. Verónica Gómez Cortés

Dr. Derek M. Stevens

Acknowledgments

Abstract

Reverse osmosis (RO) is the finest level of membrane-technology available and one of the most promising technologies to overcome the problem of global clean water scarcity. Seawater desalination currently provides approximately 50 million cubic meters per day of potable water worldwide[1]. The RO membrane market is dominated by thin-film composite (TFC) polyamide membranes consisting of three layers: a polyester web acting as structural support (120-200 μm thick), a polysulfone interlayer (about 40 μm), and an ultra-thin crosslinked polyamide layer on the upper surface (0.2 μm). Membrane pore size in the active layer is normally less than 0.6 nm to achieve salt rejection consistently higher than 99%. When operated at high temperature (max 45˚C) and high pressure (max 82 bar) membranes can suffer compaction, which results in reduced permeate production (>30%) so that the feed pressure has to be increased to meet the design parameters. Ultimately these translate into an increase in the cost of the water produced and substantially lower membrane product life-time.

The objective of this study was to gain fundamental understanding on the compaction phenomena and its implication to the transport mechanism. With that purpose a series of analyses were conducted with the aim of characterizing: (1) the membrane morphology and thickness of each layer in the membrane from cross sectional images as a result of high temperature and pressure operation, (2) the polyamide chemical content after process operation, (3) the portions of permeability flow loss due to compaction of the polyamide and support layer, separately, and their contribution to the total membrane flow loss by applying the series resistance model, and (4) the pore size (free-volume hole size) of the polyamide layer in ambient and swollen hydrated state. In total 11 different techniques were applied attempting to reveal complete information.

Several observations were identified that might be attributed to the permeability loss of the membrane after the operation. Moreover the results indicated that there is a sizable portion (>50%) of added resistance coming from the polyamide layer to the total flow loss of the entire composite

---

[1] Busch M., Accelerating Membrane Innovation, World Water, September/October p. 28-29, 2012

membrane, which leads to irreversible changes in the membrane performance. The root cause for these observations might be the changes in the polyamide network structure that most probably occurs during the operation at combined conditions of high pressure and high temperature.

The results from this work offer an important insight in the structure of thin-film composite membrane after process operation i.e. compaction and can strongly benefit in creation of novel membrane recipes, new product development and innovation.

List of acronyms

AFM	Atomic Forced Microscopy
A-value	Water permeability of membrane (gfd/psi)
B-value	Salt permeability of membrane (gfd)
DB	Doppler Broadening
ESEM	Environmental Scanning Electron Microscopy
ESCA	Electron Spectroscopy for Chemical Analysis
EDS	X-ray Energy Dispersive System
FTIR	Fourier Transform Infrared Spectroscopy
IP	Interfacial Polymerization
LC	Liquid Chromatography
MePS	Mono-energetic Positron Spectroscopy
MELT	Maximum Entropy of Lifetime
MPD	1,3-phenylenediamine
MSF	Multi-stage Flush
MS	Mass Spectrometry
NF	Nanofiltration
NMR	Nuclear Magnetic Resonance Spectroscopy
NIST	National Institute of Standards and Technology, USA
OPEX	Operating Expenses
PA	Polyamide Layer, top layer of composite membrane
PS	Polysulfone Layer
PE (PET)	Polyester Layer
PALS	Positron Annihilation Lifetime Spectroscopy

RO	Reverse Osmosis
RMR	Root mean square roughness
SWRO	Seawater Reverse Osmosis
SEM	Scanning Electron Microscopy
SAXS	Small-angle X-ray Scattering
TDS	Total Dissolved Solids
TFC	Thin-film Composite
TMC	Trimesoyl chloride
TMA	Trimesoic Acid
UV	Ultra-violet Detector
XPS	X-Ray Photoelectron Spectroscopy

Table of content

List of figures

List of tables

1 Chapter 1

This chapter is taking an overview of one of the major problems facing society in the future – clean water scarcity. The commitment to conserve and protect current water and energy resources provides the core inspiration of this research. It summarizes the basics of reverse osmosis technology as one of the most promising technologies that can offer a solution to the problem. A description of the objectives of the thesis is given as well as the organization of the subsequent chapters of this dissertation.

1.1 Introduction

1.1.1 Clean water scarcity

Water is an essential resource for life, sustainable growth and healthy ecosystems. A lack of water to meet daily needs is a reality today for one out of three people around the world. Globally, the problem is getting worse as cities and populations grow, as well as the needs for water increase in agriculture, industry and households [1]. Here are the facts that highlight the health consequences of water scarcity and its impact on daily life:

- Only 1% of water on earth is drinkable and accessible [2];
- 40% of earth's population live in water-stressed areas [3];
- Safe drinking water is not available to 1.1 billion people [1];
- 2.2 million people die each year because of contaminated drinking water [1];

"*Water scarcity is defined as the point at which the aggregate impact of all users encroaches on the supply or quality of water under prevailing institutional arrangements to the extent that the demand by all sectors, including the environment, cannot be fully satisfied*" [4]. Water scarcity is a relative concept and can occur at any level of supply or demand. Imbalances between availability and demand, the degradation of groundwater and surface water quality, intersectional competition, and interregional and international conflicts, all bring water issues to the fore [4]. It urges everyone to be part of efforts to conserve and protect this resource.
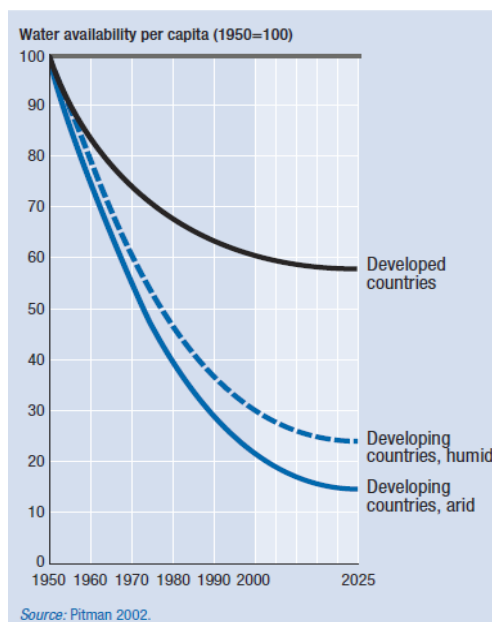
Figure 1.1. Historical and predicted water availability in decline [5]

With 1950 as a benchmark, the distribution of global population growth has dramatically reshaped the per capita availability of water. While availability stabilized in rich countries in the 1970s, the decline continued in developing countries, especially in arid developing countries (Figure 1.1). Just how rapid the decline has been becomes apparent when current trends are projected into the future. By 2025 more than 3 billion people could be living in water-stressed countries and 14 countries will slip from water stress to water scarcity [5].

1.1.2   Reverse osmosis technology

Clean water availability has become one of the major concerns for future generations. Becoming aware about water scarcity was imperative to develop technologies such as reverse osmosis (RO) for water treatment and seek for further improvement by decreasing the electrical consumption, chemical use and lower the environmental impact. Since the development of reverse osmosis as practical unit operation in late 1950's and early 1960's [6,7,8,9], the scope of their application has been continuously expanding. Today RO is the most attractive and widely used desalination technology globally. It has overtaken conventional thermal technology such as multi-stage flash (MSF) [10] and is expected to maintain its leadership in the near future, though new technologies such as membrane distillation [11], electrodialysis [12], capacitive

deionization [13] and forward osmosis [14]. Commercial interest in RO technology is increasing globally due to continuous process improvements, which leads to significant cost reduction [15]. Water demineralization with reverse osmosis membranes has also a long and successful history in industrial water treatment. Water use minimization in industrial production and power generation can be considered in two ways: (1) reducing the fresh water intake by enabling the use of alternative water sources such as municipal and industrial wastewater effluents (2) recycling water streams within the production facility itself. Nowadays increased demands on the industry to conserve water, reduce energy consumption, control pollution and reclaim useful materials from waste streams have made applications not only economically attractive, but also increasing the need to further optimize the RO water treatment system efficiency.

1.1.3   Reverse osmosis theory

Herein are given the fundamentals of the osmosis and reverse osmosis as well the concept to which the technology is based. Osmosis is a natural phenomenon in which a solvent (usually water) passes through a semipermeable barrier from the side with lower solute concentration to the higher solute concentration side. As shown in Figure 1.2, water flow continues until chemical potential equilibrium of the solvent is established. At equilibrium, the pressure difference between the two sides of the membrane is equal to the osmotic pressure difference between the solutions. To reverse the flow of water (solvent), a pressure difference greater than the osmotic pressure difference is applied; as a result, separation of water from the solution occurs as pure water flows from the high concentration side to low concentration side. This phenomenon is termed reverse osmosis (it has also been referred to as hyperfiltration) [16]. Many mechanistic and mathematical models have been proposed to describe reverse osmosis mechanism in membranes. Few of those descriptions rely on relatively simple concepts while others consider far more complex system which requires sophisticated solution techniques. Models that adequately describe the performance of RO membranes are very important since these are needed in the design of the RO process. An accurate model that predicts the membrane separation characteristics can help in reducing the number of experiments that must be performed to describe a particular system. Reverse osmosis models can be divided into three main types, given in Table 1.1 [17].
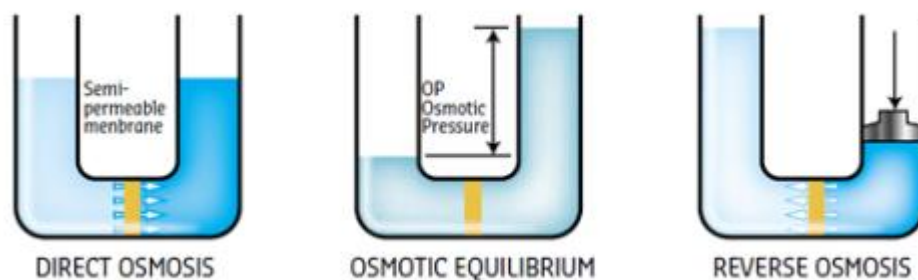
Figure 1.2. Reverse osmosis operating principle [18]

For dilute solutions, osmotic pressure is approximated using the Van't Hoff equation

$$\pi = \phi \, C_i \, RT \qquad\qquad (1.1)$$

π – Osmotic pressure [atm]
ϕ - Osmotic pressure coefficient
C_i – Molar concentration of the solute [mol/L]
R – Gas constant
T – Absolute temperature [K]

A fundamental difference exists between the assumption of the homogeneous and porous membrane models. The homogeneous models assume that the membrane is nonporous and transport takes place between the interstitial spaces of the polymer chains or polymer nodules, mainly by diffusion. The porous models assume that transport takes place through pores that run the length of the membrane barrier layer; as a result, transport can occur by both diffusion and convection through the pores [17]. More specific the solution-diffusion model assumes that: (1) the RO membrane has a homogeneous, nonporous surface layer; (2) both the solute and solvent dissolve in this layer and then each diffuses across it; (3) the solute and solvent diffusion is uncoupled and due to its own chemical potential gradient across the membrane; (4) these gradients are the result of concentration and pressure difference across the membrane. Differences in the solubilities (partition coefficients) and diffusivities of the solute and solvent in the membrane phase are extremely important in this model since these strongly influence fluxes through the membrane [17].

The fundamental equations for water and solute transport considering the solution-diffusion model are:

Water flux: $J_w = k_w(\Delta P - \Delta \pi) = k_w[(P_F - P_P) - (\pi_F - \pi_P)]$ (1.2)

J_w – Solvent flux [gfd]
k_w – Solvent permeability [gfd/psi], also referred as A-value
ΔP – Transmembrane pressure differential [psi]
$\Delta \pi$ – Osmotic pressure differential [psi]

Solute flux: $J_s = k_s \cdot \Delta C$ (1.3)

J_s – Solute flux [lbfd]
k_s – Solute permeability [gfd], also referred as B-value
ΔC – Transmembrane concentration differential [lb/gal]

Table 1.1. Reverse Osmosis Theory Models

	Type	Model	Relevant references
1	Irreversible thermodynamic models	Kedem-Katchalsky Spiegler-Kedem	[19][20][21] [22]
2	Non porous or homogenous membrane models	Solution-diffusion Solution-diffusion-imperfection Extended solution-diffusion	[23][24] [25] [26]
3	Pore models	Finely-porous Preferential sorption-capillary flow Surface force-pore flow models	[27][28] [29][30] [31][30]
Other	Charged membrane models for RO (i.e nanofiltration)	Donnan Equilibrium Extended Nernst-Planck	[24][32] [33][34]

1.1.4 Reverse osmosis membrane and their system arrangement

Reverse osmosis is the finest level of membrane-technology filtration available. The RO membrane acts as a barrier to all dissolved salts and inorganic molecules, as well as organic molecules with a molecular weight greater than approximately 100 Da (Figure 1.3). Water molecules, on the other hand, pass freely through the membrane creating a purified product stream. Rejection of dissolved salts ranges from 95% to greater than 99.5% [35].
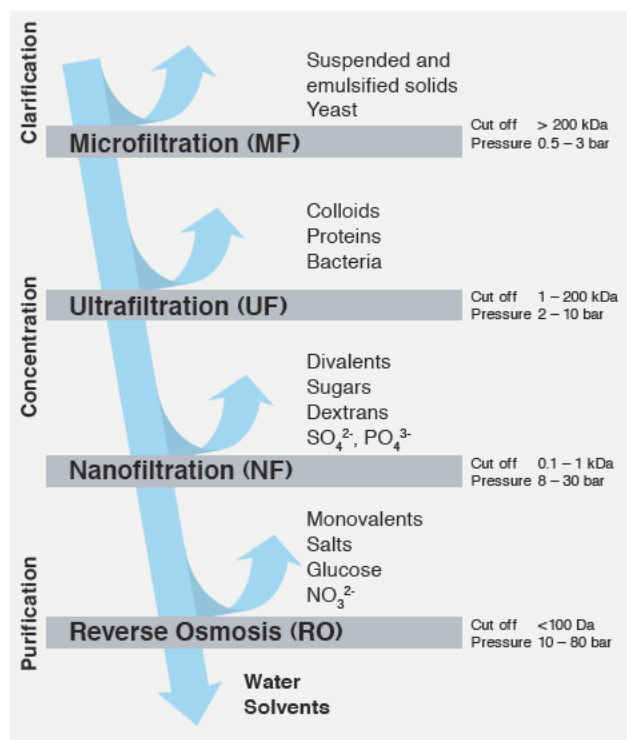
Figure 1.3. Membrane filtration spectrum [36]

The RO membrane market is dominated by thin film composite (TFC) polyamide membranes consisting of three layers (Figure 1.4), a polyester web acting as structural support (120-200 μm thick), a microporous polysulfone interlayer (about 40 μm), and an ultra-thin polyamide barrier layer on the upper surface (0.2 μm) [37]. Membrane pore size in the active layer is normally less than 0.6 nm to achieve salt rejection consistently higher than 99%. [15] The selective barrier layer is most often made of aromatic polyamide, for example via interfacial polymerization of 1,3-phenylenediamine (MPD) and trimesoyl chloride (TMC) [38].

24

The performance of the membrane is manly determined by the monomers used in the interfacial polymerization. Even small changes in the monomer structure and concentration can strongly influence the membrane properties. The membrane performance and morphology is dependent on several synthesis conditions, such as concentration of reactants, reaction time and post treatments of the resulting films [39]. Moreover, the surface roughness and pore dimension of the support layer also have significant effects on the formation of the interfacial film. Generally, a smooth surface may favor the formation of a thick defect-free active layer. The resultant composite membrane will give high salt rejection and low flow. On the other hand, a rough surface may result in a thin active layer with some defects. So the composite membrane may have higher flux with a little sacrifice of salt rejection [40,41]. Surface modification has commonly been used to further improve membrane performance of the prepared membranes. Some of the techniques include surface functionalization, cross-linking, grafting and coating [42].

Schematic cross-section of a thin-film membrane used in reverse osmosis

Support layer
Polysulphone (PS)

Thin-film membrane layer
Polyamide (PA)

Support paper
Polyester (PE) or
polypropylene (PP)
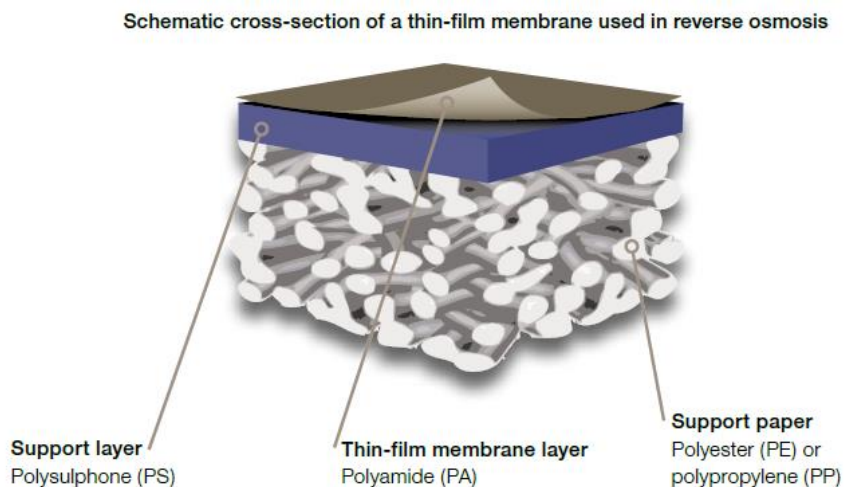
Figure 1.4. Schematic cross-section of a thin-film membrane [35]
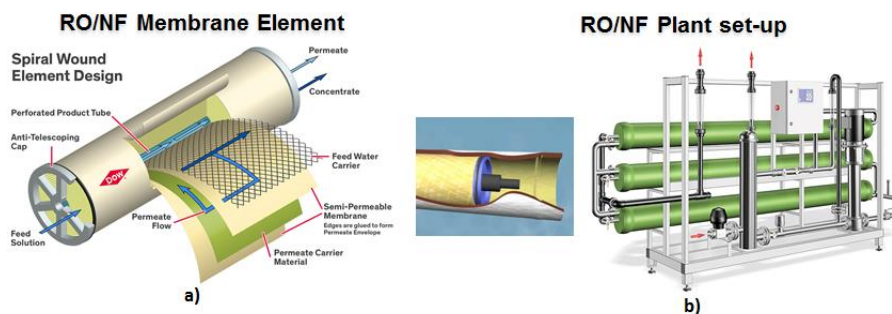
Figure 1.5. Schematic of a) RO spiral wound element design and b) RO pilot plant set-up [35]

Typically membranes are packed in a spiral wound configuration (Figure 1.5 a). Spiral wound designs offer many advantages compared to other module designs, such as tubular, plate and frame and hollow fiber module design for most of the reverse osmosis applications in water treatment. A spiral wound configuration offers significantly lower replacement costs, simpler plumbing systems, easier maintenance and greater design freedom than other configurations, making it the industry standard for reverse osmosis and nanofiltration membranes in water treatment.

Standard 8-inch diameter element contains 26-28 membrane leaves. Each membrane leaf is made of two membrane sheets glued together back-to-back with a permeate spacer in-between them. Automated manufacturing process produces consistent glue lines about 1.5 inch (4 cm) wide that seal the inner (permeate) side of the leaf against the outer (feed/concentrate) side. There is a side glue line at the feed end and at the concentrate end of the element, and a closing glue line at the outer diameter of the element. The open side of the leaf is connected and sealed against the perforated central part of the product water tube, which collects the permeate from all leaves. The leaves are rolled up with a sheet of feed spacer between each of them, which provide the channels and exits on the opposite end as concentrate. A part of the feed water, typically 10-20%, permeates through the membrane into the leaves and exits the permeate water tube [35].

When elements are used for high permeate production rates, the pressure drop of the permeate flow inside the leaves reduces the efficiency of the element. Therefore the elements have been optimized with a higher number of shorter leaves and thin and consistent glue line. The current construction further optimizes the actual active membrane (the area inside the glue lines)

and the thickness of the feed spacer. Element productivity is enhanced by high active area while a thick feed spacer reduces fouling and increases cleaning success [35].

In membrane systems the elements are placed in series inside of a pressure vessel that are arranged in a certain manner (Figure 1.5 b). The concentrate of the first element becomes the feed to the second element and so on. The permeate tubes are connected with interconnectors (also called couplers), and the combined total permeate exits the pressure vessel at one side (sometimes at both sides) of the vessel.

There are a handful of calculations that are used to judge the performance of an RO system and also for design consideration. For instance:

- **Permeate flux** - the rate of permeate transported per unit of membrane area:

$$J_w = \frac{Volumetric\ or\ mass\ permeation\ rate}{membrane\ area} \qquad (1.4)$$

Permeate flux is sometimes normalized to the initial or pure water flux (J_{wo}) as $\frac{J_w}{J_{wo}}$ or as flux drop, defined by:

$$Flux\ Drop = 1 - \frac{J_w}{J_{wo}} \qquad (1.5)$$

- **Recovery** – the percentage of membrane system feedwater that emerges from the system as product water or permeate:

$$Recovery\ (\%) = \frac{Permeate\ flow\ rate}{Feed\ flow\ rate} \cdot 100 \qquad (1.6)$$

- **Salt Passage** - the percentage of dissolved constituents (contaminants) in the feedwater allowed to pass through the membrane:

$$Salt\ Passage\ (\%) = \frac{Permeate\ Salt\ Concentration}{Feed\ Salt\ Concentartion} \cdot 100 \qquad (1.7)$$

- **Salt rejection** -the percentage of solids concentration removed from system feedwater by the membrane, opposite of salt passage:

$$Salt\ Rejection\ (\%) = 100 - Salt\ passage \qquad (1.8)$$

1.1.5   Future developments and challenges for RO

In the future the needs for seawater desalination and water reuse will continue to increase. The primary limitation to further application of RO is the cost for the energy consumption which represents the major portion (44%) of the total cost of water desalination [43]. In that sense the novel strategy must offer a possible solution to the problem satisfying the increasing demand for water, energy, raw materials and products under constrains imposed by the concept of sustainable development. Here are some key factors for improving:

- New membrane modules and materials particularly adapted to water treatment with enhanced transport mechanisms, selectivity, flux;
- Development of membranes with higher thermal stability and higher chemical resistance and stability (for example chlorine);
- Optimization of system design for achieving the most increasingly stringent water quality standards with respect to new contaminants or micro pollutants;
- Development of water treatment systems coupled with renewable energy sources for a significant reduction in energy consumption and in the dependence on fossil fuel;
- Novel concentrate treatment options (such as membrane crystallization).

1.1.6   Market overview

By 2030, under an average economic growth scenario and without efficiency gains, global water requirements will grow from 4,500 billion cubic meters today to 6,999 billion cubic meters – a 50 percent increase in just two decades [44]. Analysts predict that available water supplies will satisfy only 60 percent of demand. Demand for water continues to grow as a result of increasing population, urbanization and higher living standards. Current projections also indicate market growth in all water applications segments, such that water treatment will become a $30 billion industry by 2025 (Figure 1.6).
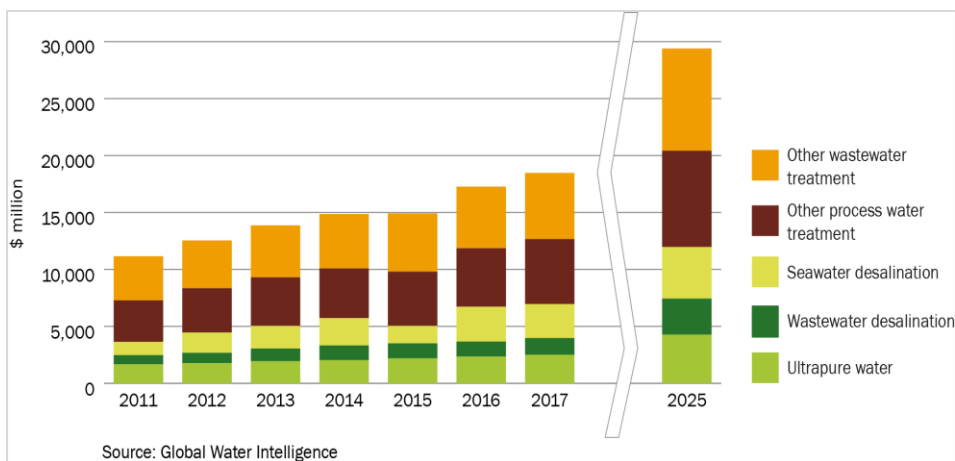
Figure 1.6. Market Forecast by Major Market, Source: Global Water Intelligence [44]

1.1.7   Research interest

A literature research was carried out to review experience with reverse osmosis membranes and their application for seawater desalination. Today the most relevant journals are (journal's impact factor for 2013): Journal of Membrane Science (4.90), Desalination (3.96), Separation and Purification Technology (3.06), Water Research (5.32), Water Science and Technology (1.21) and Desalination and Water Treatment (0.98).

The key words "reverse osmosis membrane" were searched with the automatic search engine available from Web of Science Core Collection [45]. The search was performed and evaluated for all sources available up to February 2016, including journal and book publications for all times. The earliest records were dated from 1965. The search yielded 1,634 records in total and the latest 20 years are displayed on Figure 1.7 a. Exponential growth is noticed only in the last 10 years which means that RO became an emerging technology in that period and more research teams were engaged to work for further development of this field. Analogous to the increase in published items the citation of those increased and the sum of times cited without self-citations was 23,230 (Figure 1.7 b) with average citation per item of 17.5.

29
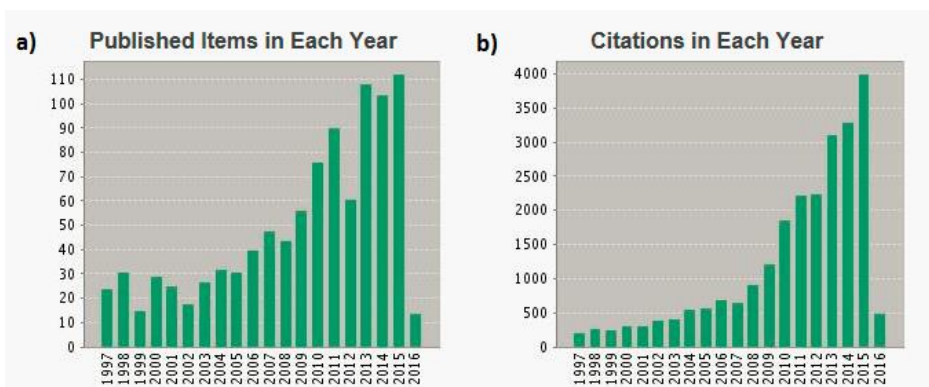
Figure 1.7. Web of Science searching engine results displaying the latest 20 years: a) Publishing items in each year and b) Number of citations in each year

1.2 Description of the thesis objective

The scope of this study is a phenomenon known as compaction. Several definitions about compaction are given below, collected from different sources/manufacturers of membranes:

a) Membrane compaction refers to the physical compression of the RO membrane itself. This compression results in a decrease in flux. The rate of compaction is directly proportional to an increase in temperature and pressure [46].

b) The decrease in membrane water permeability as the pressure in the membrane increases [47].

c) Operation at temperatures exceeding 45˚C may results in compaction of the polysulfone support layer. Membrane compaction reduces permeability, resulting in higher feed pressure to maintain permeate flow [48].

d) Membrane compaction and intrusion is typically associated with low permeate flow and improved salt rejection. Compaction is the result of applied pressure and temperature compressing the membrane which may result in a decline in flux and salt passage. Intrusion is the plastic deformation of the membrane when pressed against the permeate channel spacer under excessive forces and/or temperatures. The pattern of the permeate spacer is visibly imprinted on the membrane. Intrusion is typically associated with low flow. In practice, compaction

30

and intrusion may occur simultaneously and are difficult to distinguish from each other [35].

e) Exposure of membranes to high pressure may result in an increase in the density of membrane material (called compaction), which will decreases the rate of diffusion of water and dissolved constituents through the membrane. As a result of compaction, higher pressure has to be applied to maintain the designed permeate flow. In parallel, a lower rate of salt diffusion will result in lower permeate salinity. The effect of compaction is more significant in asymmetric cellulose membranes than in composite polyamide membranes. In seawater RO, where the feed pressure is much higher than in brackish applications, the compaction process will be more significant. Higher feed water temperature will also result in a higher compaction rate. Usually membrane compaction results in few percent flux decline, and has strongest effect during the initial operating period [49].

All definitions given above share the consequences of compaction, i.e. the changes seen in the performance without giving clear explanation and insight of the changes experienced by each layer (down to molecular level) and its implication to the water transport through the membrane. Moreover there is no clear agreement on whether the high pressure, the high temperature, or both simultaneously contribute strongly to the compaction. In reality we know that the higher pressure is conditioned by the feed water TDS (Total Dissolved Solids), i.e. osmotic pressure, while the feed temperature will depend on the local characteristics of the feed water and application. Additional complexity is required to describe the changes experienced by each layer individually and how this translate to the final performance of the thin film composite membrane observed in the field. For instance, some of the definitions above refer to changes in the polysulfone layer without mentioning effect of compaction on the polyamide active layer. Furthermore, improved salt rejection is indicated as second observation after the flow loss as outcome of compaction. However in real practice the compaction is not an isolated phenomenon and can appear simultaneously with intrusion and fouling (Figure 1.8). Thus there might be few causes for flux decline coming from different origins. It's extremely difficult to segregate and quantify each portion that contributes to total amount of permeate flow loss. Moreover some authors [50] are going step forward and are talking about two portions for the total flow loss: (1) reversible portion – partially reversible portion in flow noted after the elements are out of operation or stored for some time (from several hours

to few days), but irreversible when the elements continues to operate. It is also referred as "rebound effect" and (2) irreversible portion – it is portion of the flow that cannot be recovered in any way for the reasons that are not well understood yet.

The first theoretical and experimental explanation for compaction of cellulose acetate membrane was given by Joel L. Bert in 1969 [47]. Nine years later Haruhiko Ohya [51] gave an expression method for the compaction effect on reverse osmosis membranes at high pressure operation for the purpose of precisely predicting their life over a long term.

For large industrial scale plants the compaction of the elements results in reduced permeate production so that the feed pressure has to be increased to meet the design parameters. Ultimately, this translates into an increase in operating expenses (OPEX) due to the higher energy/electricity requirements and substantially shorter product life-time.

Nevertheless the current knowledge available is still very limited with no deep insights in the structure of the thin film composite membranes. Thus the objective of this thesis is to gain fundamental understanding about the compaction phenomenon. The investigation here is considering all membrane layers, but with strong focus on the polyamide layer.

The main research hypothesis in this study is that some of the irreversible flow reduction in compaction is due to structural changes in the PA network. The statement by itself is opposite to general belief, because the PA is considered to have a very stable structure that is not affected within the typical operating range (temperature up to 45˚C and pressure up to 82 bar). Moreover the PA is not soluble in many common solvents and thus provides a unique challenge to conventional analytical chemistry methods. Until now there is a lack of experimental results that will confirm or deny this hypothesis. Thus the focus of this research was to set up a series of analysis in order to identify and describe any structural changes in the PA chemistry. The effects of intrusion and fouling are confounding variables with compaction but are not a focus of this work. In total 11 different techniques were applied, divided and listed in four blocks in Table 1.2. Each of the techniques used will be described, followed by results discussion in the subsequent chapters of this dissertation.

It is important to mention that all membranes analyzed are seawater reverse osmosis membranes (except in chapter five where nanofiltaration membrane

D by Dow FILMTEC™[2], Minneapolis, was used as control sample). As the operating pressure in seawater desalination application is higher, seawater membranes are considered more prone to compaction compared to brackish or nanofiltration membranes operated under brackish or nanofiltration feed pressures.

Table 1.2. Phase's overview with list of the analytical techniques applied

Phase	Description	Analysis	Place
I	Analysis on the membrane surface structure and morphology description; cross section and thickness measurement	Atomic Force Microscopy	Universitat Rovira i Virgili
		Scanning Electron Microscopy	
		Environmental Scanning Electron Microscopy	
II	Characterization of the membrane chemical content before and after operation (post compaction)	X-ray Photoelectron Spectroscopy	Dow Core R&D, Midland
		Fourier Transform Infrared Spectroscopy	
		Variety of analysis that combine more than one technique	
III	Flat Cell Experimental Analysis; Segregate the total flow loss between its constituent (PA and PS)	A-value Composite A-value Polyamide A-value Support	DW&PS R&D, Edina
IV	Data for the pore size and distribution can be generate in order to describe the implication of the microstructure to filtration and transport mechanism	Positron Annihilation Lifetime Spectroscopy	Helmholtz-Zentrum Dresden-Rossendorf, Germany

---

[2] ™Trademark of The Dow Chemical Company ("Dow") or an affiliated company of Dow
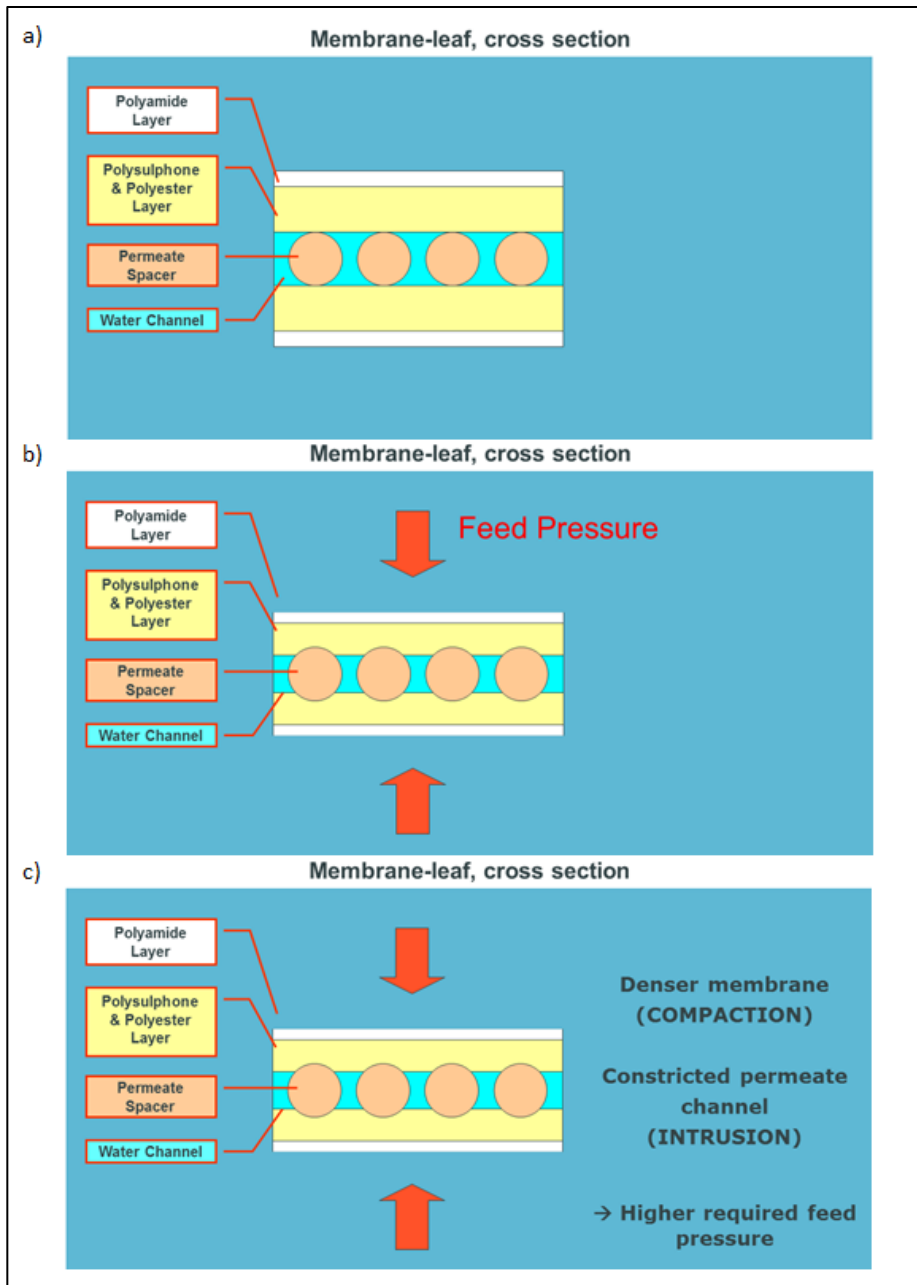
Figure 1.8. Simplified drawing to depict the compaction and intrusion: a) New membrane; b) Membrane in operation under certain feed pressure c) Compacted membrane after operation

1.3 Evidence of compaction in a long-term operation

As mentioned earlier the compacted samples studied in this thesis were collected after long-term process operation in an RO pilot plant set-up. The two main parameters used to judge the performance of an RO system are the production rate and the quality of the permeate being produced. Depending of the interest other parameters might be studied like energy savings, fouling resistance, cleanability etc.

One representative case was chosen to describe the evidence of compaction during the long-term process operation at conditions that combines elevated temperature and pressure together. The assessment of the membranes in spiral wound configuration typically goes through several stages:
- Individual pre-test of the elements
- Long term operation
- Individual post-test of the elements
- Chemical cleaning and/or autopsy
Here as point of interest will be covered only the first three stages. The objective of the experiments presented here was to quantify the long term flow and rejection performance of membrane A. The element with serial number F9279785 was used after autopsy to collect sample.

1.3.1 Experimental procedure

Details for the experimental set up and operating conditions during the trial are presented in this section.

1.3.1.1 RO pilot plant

The long term operation took place in the Dow Water & Process Solutions Global Water Technology Center in Tarragona, Spain. The utilized pilot plant is equipped with six pressure vessels divided in two lines RO 1 and RO 2, each with three pressure vessels and three positions for elements per vessel (Figure 1.9). The vessels can be connected in series or in parallel depending on the requirements. Prior to the RO system there is a ultrafiltration (UF) section as pretreatment, the water filtrate outcome the UF is collected in UF filtrate tank from where with low pressure pump is carried to the cartridge filter with a pore size of 5 µm (it helps to prevent the subsequent high pressure pump and RO elements from suspended particle). The injection points of antiscalant and the sodium metabisulphide (SMBS) are located between the cartridge filter and high pressure pump that prevent the RO from scale formation and

oxidation respectively. The water from the high pressure pump is distributed to the different pressure vessels of the RO section.
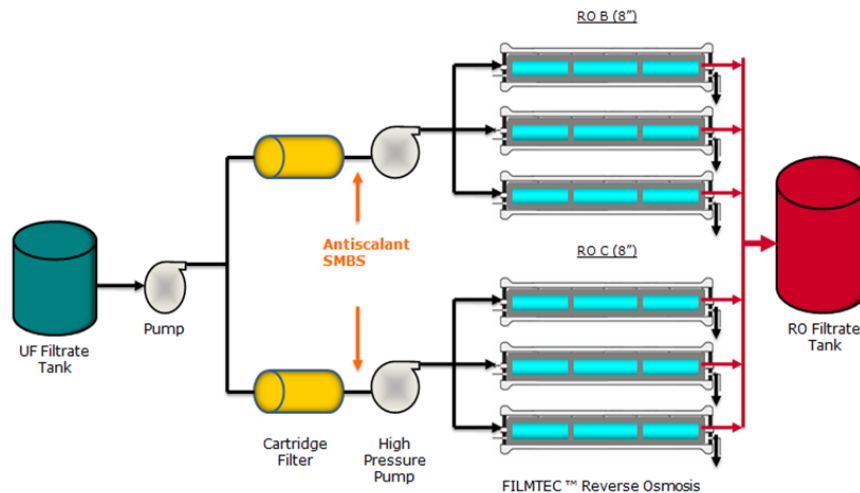
Figure 1.9. Large Asset Reverse Osmosis Pilot Plant

1.3.1.2   Operation strategy

Three operational phases were completed with conditions given in Table 1.3:

Phase 1 – four days in normal operation with environmental feed temperature;

Phase 2 – one month in recirculation with synthetic NaCl solution;

Phase 3 – four days in normal operation with environmental feed temperature.

The stable parameters during the operation were the feed pressure and feed flow.

Table 1.3. Operating conditions per phase

Phase	Phase 1	Phase 2	Phase 3
Step	Standard	High 1	Standard
Feed TDS (mg/l)	32,000	48,000	32,000
Temperature (°C)	25	40/43	25
Flux (lmh)	15	15	15
Recovery (%)	30	30	30
Duration (days)	4	30	4

1.3.2 Data collection and normalization

Performance monitoring of the RO process is very important to ensure sustainable operation of the system. It helps to track the different performance trends, decide when to clean or replace membranes. It gives also useful information in troubleshooting or in event of warranty claim.

Normalization is a calculation method to express measured membrane performance variables in terms of a set of reference conditions. This allows the user to determine whether observed changes in membrane performance (flow and/or rejection) are normal variation due to a change in operating conditions or may be an indication of fouling, scaling or damage to the membrane. Typical reference conditions are the stabilized start-up performance data or the computer model (ROSA –Reverse Osmosis System Analysis) [52] projected performance at standard conditions or start-up performance conditions. Normalization eliminates the effect of fluctuating operating conditions and allows monitoring of the membrane properties.

The raw data were normalized using the R&D version of FT-NORM, a spreadsheet based analysis routine provided by FILMTEC™[3]. The normalization was customized to calculate osmotic pressure using real feed and permeate water composition, rather than the sodium chloride equivalent approach used in the current commercial version of FT-NORM [53]. In addition the given equations were used to calculate the apparent system A-value and its ratio:

$$A - value' = \frac{Raw\ Flux\ (lmh)}{NDP(bar) * TFC(A - value)} \qquad (1.9)$$

$$Ratio = \frac{A - value'(real)}{A - value'(reference)} \qquad (1.10)$$

where NDP is the net driving pressure of the system and TFC the temperature correction factor.

ROSA projected performance for start-up was used as the reference line. It considered 50 bar of feed pressure, 6.30 m^3/h feed flow per vessel, 25°C temperature, 50,000 μS/cm feed conductivity (78,000 μS/cm for the high pressure stage), 15 lmh flux and 30% recovery.

---

[3] ™Trademark of The Dow Chemical Company ("Dow") or an affiliated company of Dow

1.3.3   Operating performance summary

Figure 1.10 a) gives the ratio of the real A-value versus the reference A-value (is worth mentioning that in this case we are speaking about A-value calculated for three elements in series). For a new element this ratio should be between 0.90-1.00. The first operation phase considers conservative operation on 25°C and 50 bar, and the elements indeed provide the expected permeate rate. The ratio appears lower on 40/43°C and 70 bar, because the reference normalization line is same as before (25°C and 50 bar). When going back to normal operation after the combined high temperature with high pressure operation we can see that the ratio decreased to 0.60, which makes almost 30% of permeate flow loss. However, not all the portion of flow loss is due to compaction. Fouling and intrusion appears simultaneously and is extremely difficult to segregate the flow loss portion coming from each. Portion of the flow will be eventually recovered after chemical cleaning.

Figure 1.10 b) give the real permeate conductivity and the one projected by the ROSA program. In fact ROSA output is generating the permeate TDS and factor of 2.0 was used to get the projected permeate conductivity in µS/cm. In general no significant difference is noticed between the operation before and after compaction.

The individual standard test done on the elements before and after operation just confirms on the flow loss seen during the system operation (Figure 1.11).
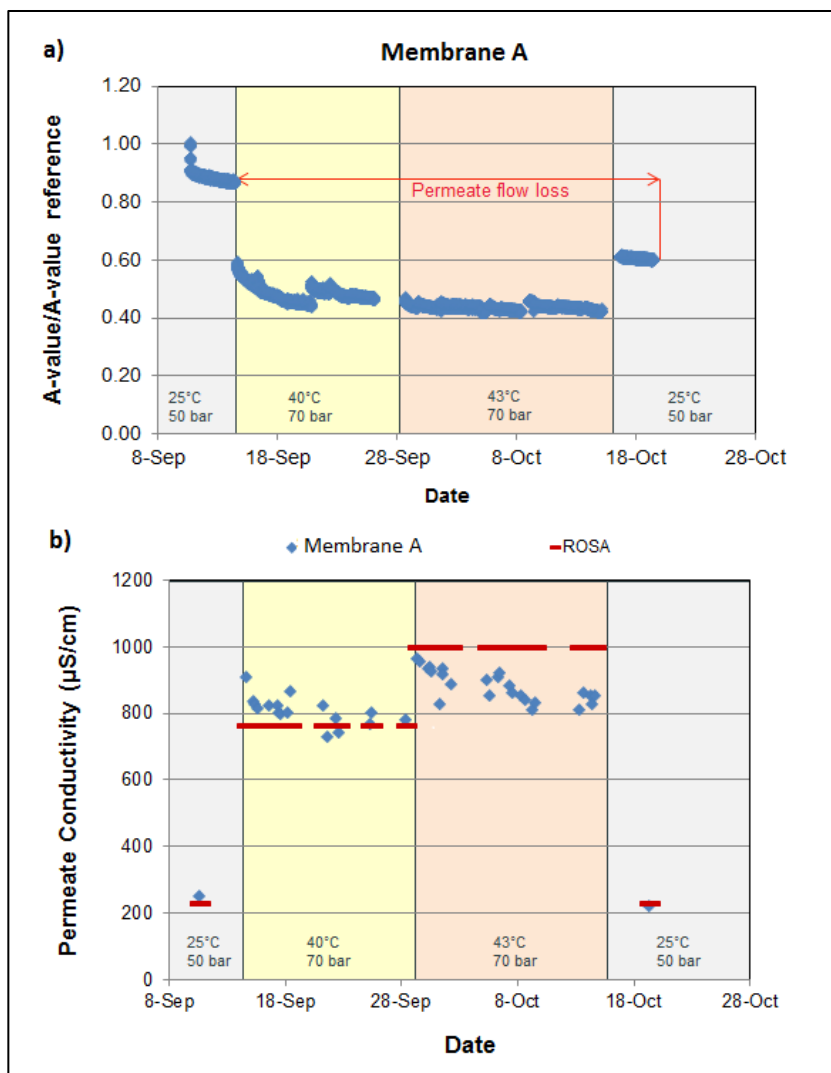
Figure 1.10. Long-term performance of membrane A a) A-value ratio b) Permeate conductivity

Figure 1.11. Individual element performance before and after the long-term operation

1.3.4 Impact of the compaction

In reality the end-user in large scale RO installations will perceive the effect of compaction as a need to increase the feed pressure of the system in order to maintain the desired production rate. This implies an increase in the energy/electricity requirements to run the high pressure pump. After several consequent increases the operation will be no longer efficient, the operating costs would be higher and thus replacement of the elements will be needed. Consequently, compaction may affect the sustainable operation of the RO system considerably.

1.4 References

[1]. World Health Statistics (2009) World Health Organization, WHO Press, Geneva, Switzerland

[2]. Human Appropriation of the World's Fresh Water Supply. (2006) Global Change Program: University of Michigan, accessed 08.12.2015. http://www.globalchange.umich.edu/globalchange2/current/lectures/freshwater_supply/freshwater.html.

[3]. Food and Agriculture Organization of the United Nations (2012) *FAO Statistical Yearbook.*

[4]. Coping with Water Scarcity, Challenge of the Twenty-first Century (2007) United Nations.

[5]. Human Development Report, Water scarcity, risk and vulnerability, chapter 4. (2006) United Nations Development Programme.

[6]. Reid, C.E., Breton E.J. (1959) Water and ion flow across cellulosic membranes. *Journal of Applied Polymer Science* 1*,* (2), 133-143.

[7]. Reid, C. (1966) Principles of Reverse Osmosis. In *Desalination by Reverse Osmosis.* U.Merten, ed. *(*pp. 1-14), M.I.T. Press, Cambridge, Mass.

[8]. Loeb, S. Sourirajan, S**.** (1963) Sea water demineralization by means of an osmotic membrane. *Advances in Chemistry Series* 38, 117-132.

[9]. Loeb, S. (1981) The Loeb-Sourirajan membrane: how it came about. In *Synthetic Membranes.* Turbak A., ed. (pp. 1-9) Vol. 153, ITT Rayonier. Inc.

[10]. Energy Makes All the Differece: Desalination Operating Costs Compared-Chart (2007) Global Water Intelligence.

[11]. Hsu, S.T, Cheng K.T., Chiou J.S. (2002) Seawater desalination by direct contact membrane distillation. *Desalination* 143, 279-287.

[12]. Sadrzadeh, M. and Mohammadi, T. (2008) Sea water desalination using electrodialysis. *Desalination* 221, 440-447.

[13]. Oren, Y. (2008). Capactive deionization (Cdi) for desalination and water treatment-past, present and future*. Desalination* 228, 10-29.

[14]. McGinnis, R.L., Elimelech, M. (2007) Energy requirements of ammonia-carbon dioxide forward osmosis desalination. *Desalination* 207, 370-382.

[15]. Lee, K.P., Arnot, T.C., Mattia. D. (2011) A review of reverse osmosis membrane materials for desalination-development to date and future potential. *Journal of Memebrane Science* 370, 1-22.

[16]. Williams, M.E. (2003) A brief review of reverse osmosis membrane technology*,* white paper. EET Cprporation and Williams Engineering Services Company, Inc.

[17]. Williams, M.E. (2003) A review of reverse osmosis theory*,* white paper. EET Cprporation and Williams Engineering Services Company, Inc.

[18]. Degremont Industry, available from:
http://www.degremont.com/en/know-how/municipal-water-
treatment/desalination/reverse-osmosis/processes/; accessed 09.12.2015

[19]. Kedem, O., Katchalsky, A. (1958) Thermodynamic analysis of the
permeability of biological membranes to non-electrolytes. *Biochimica et
Biophysica Acta* 27, (2), 229-246.

[20]. Jonsson, G. (1980) Overview of theories for water snd solute transport in
UF/RO membranes. *Desalination* 35, 21-28.

[21]. Soltanieh, M., Gill, W**.** (1981) Review of reverse osmosis membranes and
transport models*. Chemical Engineering Communications* 12, 279-363.

[22]. Spiegler, K., Kedem, O. (1966) Thermodynamics of hyperfiltration (reverse
osmosis): criteria for efficient membranes*. Desalination* 1, (4), 311-326.

[23]. Lonsdale, H., Merten, U. Riley, R. (1965) Transport properties of cellulose
acetate osmotic membranes. *Journal of Applied Polymer Science* 9, 1341-1362.

[24]. Bhattacharyya, D., Williams, M. (1992) Theory-Reverse Osmosis. In
Membrane Handbook. Ho W., Sirkar K. ed. (pp. 269-280), Van Nostrand
Reinhold, New York

[25]. Sherwood, T., Brian, P. and Fisher, R.(1967) Desalination by reverse
osmosis. *Industrial and Engineering Chemistry Fundamentals* 6, 2-12.

[26]. Burghoff,H.G., Lee, K.L., W., Pusch. (1980) Characterization of transport
across cellulose acetate membranes in the presence of strong solute-
membrane interactions. *Journal of Applied Polymer Science* 25, (3), 323-347.

[27]. Merten,U. (1966) Transport Propoerties of Osmotic Membranes. In
Desalination by Reverse Osmosis. U.Merten, ed. (pp. 15-54) MIT Press,
Cambridge.

[28]. Jonsson*,* G., Boesen, C. (1975) Water and solute transport through
cellulose acetate reverse osmosis membranes. *Desalination* 17, 145-165.

[29]. Sourirjan, S. (1970) Reverse Osmosis . Academic Press, New York.

[30]. Sourirajan, S., Matsura, T. (1985) Reverse osmosis/ultrafiltration
principles*.* National Research Council, Ottawa.

[31]. Sourirajan, S., Matsura, T. (1981) Reverse osmosis transport through
capillary pores under the influence of surface forces. *Industrial and Engineering
Chemistry Process Design and Development* 20, 273-282.

[32]. Bhattacharyya, D., Cheng, C. (1986) Separation of metal chelates by
charged composite membranes. In *Recent Developments in Separation Science
9 .* N. Li, ed. (pp. 707) CRC Press, Boca Ration, FL

[33] Lakshminarayanaiah, N. (1965) Transport phenomena in artificial
membranes. *Chemical Reviews* 65, (5), 491-565.

[34]. Dresner, L., Johnson, J. (1980) Hyperfiltration (reverse osmosis). In
Principles of Desalination. K. Spiegler, A.Laird, ed. (pp. 401-560) Academic
Press, New York

[35]. The Dow Chemical Company, FILMTEC Reverse Osmosis Membranes, technical manual, p. 181, Midland, http://www.dow.com/scripts/litorder.asp?filepath=/609-00071.pdf.

[36]. Sluzer Management Ltd, Winterthur,Switzerland. Available from: https://www.sulzer.com/en/Products-and-Services/Separation-Technology/Membrane-Technology/Membrane-Separation-in-Acqueous-Environment; accessed 11.12.2015.

[37]. Petersen, R.J., Cadotte J.E. (1990) Thin film composite reverse osmosis membrane. In *Handbook of Industrial Membrane Technology.* M.Porter, ed. (pp. 307-348), Noyes Publication, Park Ridge, NJ

[38]. Cadotte J.E. (1977) Reverse Osmosis Membrane. US Patent 4,039,440.

[39]. Wu, C., Zhang, S., Yang, D., Wei, J.,Yan, C., Jian,X. (2006) Preparation, characterization and application in wastewater treatment of a novel thermal stable composite membrane. *Journal of Membrane Science* 279, 238-245.

[40] Weis, A., Bird, M.R., Nystrom M., Wright, C. (2005) The influence of morphology, hydrophobicity and charge upon the long-term performance of ultrafiltration membranes fouled with spend sulphite liquor. *Desalination* 175, 73-85.

[41]. Van der Bruggen, B., Manttari, M., Nystom, M. (2008) Drawbacks of applying nanofiltration and how to avoid them. *Separation and Purification Technology* 63, 251-263.

[42] Chaoyi, Ba. (2010) Design of advanced reverse osmosis and nanofiltration membranes for water purification. PhD Thesis, University of Illinois, Urbana.

[43]. Desalination and Water Purification Technology Roadmap (2003) Sandia National Laboratories and the U.S. Department of Interior, Bureau of Reclamation.

[44]. The 2030 Water Resources Group. (2013) Charting our Water Future: Economic Frameworks to inform Decision-Making. Washington, DC.

[45]. Thomson Reuters, Web of Science™, www.thomsonreuters.com.

[46]. Reverse Osmosis Chemicals. Available from: Reverse Osmosis Chemicals International. http://reverseosmosischemicals.com/reverse-osmosis-guides/reverse-osmosis-glossary-terms/membrane-compaction-reverse-osmosis-systems, accessed 15.12.2015.

[47]. Bert, Joel L. (1969) Membrane compaction: a theoretical and experimental explanation. *Polymer Letters* 7, 685-691.

[48]. LG NanoH2O (2013) Quantum Flux Seawater Reverse Osmosis Element, Technical Manual.

[49]. A Nitto Denko Corporation (2001) Design Parameters Affecting the Performance.

[50]. Gorenflo, A., Marsh,T., Busch, M. (2007) Aspect of High Temperature Operation with Spiral Wound SWRO Membrane Elements, IDA World Congress-Mas Palomas, Gran Canaria – Spain, October 21-26,. REF: IDAWC/MP07-168.

[51]. Ohya, H. (1978) An expression method of compaction effects on reverse osmosis membrane at high pressure operation. *Desalination* 26, 163-174.

[52]. The Dow Chemical Company, ROSA v 9.1, Midland, 2016. Available from: http://www.dowwaterandprocess.com

[53]. The Dow Chemical Company, FT-NORM, Midland, 2016. Available from: http://www.dowwaterandprocess.com

2   Chapter 2

The physical changes of the seawater reverse osmosis membrane after compaction were observed under different microscopic techniques. This chapter provides an insight in parameters like surface roughness, top and bottom side morphology and membrane thickness. The analytical techniques applied for this purpose were Atomic Force Microscopy (AFM), Scanning Electron Microscopy (SEM) and Environmental Scanning Electron Microscopy (ESEM). This chapter includes the experimental challenges found, results interpretation and discussion for each of them.

2.1 Analytical Part I - Microscopic analysis

The performance of polyamide composite reverse osmosis membranes is essentially determined by a dense top layer several hundred nanometers thick. Improved understanding of this critical thin layer will likely advance our knowledge and help to control membrane properties (like permeability, fouling, rejection of uncharged chemicals, trace organics etc.) [1]. Because atomic force microscopy (AFM) has the ability to image surfaces with atomic resolution, many researchers have used it to study membrane surface properties [2]. The major efforts were to ascertain if there is a universal relationship between membrane surface roughness and flux. So far contradictory findings have been reported by different groups and the effect of surface roughness on RO membrane flux is not yet clear and further studies are needed in this direction. Below are summarized some:

In 1996, Hirose suggested an approximately linear relationship between membrane surface roughness and flux for cross-linked aromatic polyamide RO membrane [3]. Kwak and Ihm in study from 1999 reported that the membrane performance depends preliminary on the nature of the thin film layer. The improved performance was correlated with the change in the inherent material property of the active layer particularly in the wet state. The relaxation behavior and the molecular motion of the wet thin film polymers were characterized by nuclear magnetic resonance spectroscopy (NMR), and it was found that the local polyamide chain motion plays a critical role in RO permeability [4]. Two years later Madaeni showed that the rougher the membrane the lower the permeation rate due to the adsorption and trapping of the ions on the rough surface membrane [5]. According to Ghosh et al. in the MPD-TMC (*m*-phenylenediamine – trimesoyl chloride) membranes neither film thicknesses nor morphology are intrinsically related to water permeability. Permeation may occur at a "dense inner barrier layer" and the visible surface morphology is an unfortunate byproduct of the polymerization reaction [6]. Therefore the major factors that affect the morphology are the organic solvent properties (amine monomer solubility and diffusivity), use of combination of additives, solvent temperature during polymerization, other reaction conditions and curing conditions.

Moreover there are several common challenges related with AFM analysis on membranes:

- High variation in surface roughness: RO membrane surface is not uniform and plane, results shown that studying images from different areas of one membrane resulted in up to 33% variation in surface roughness [2].

- Gaining representative values out of very small surface (5 x 5 μm): Typical industrial sized elements are 37-40 m^2. Taking into account the variation in the surface and the difference between the membrane and sample sizes some statistics approach might be required to ensure representative results.
- Dry versus wet conditions: Membrane surface morphology changes upon exposing the membrane to different environments and so the condition under which the roughness is measured is very important. Results presented by Al-Jeshi shows that the membrane surface roughness increased by 35% after 2h soaking in water [2]. In our case we were always working with dry membranes.
- Coated membranes: Effective roughness of the RO membrane might be reduced upon coating due to non-uniform and non-continuous characteristics that coating has.
- Fouling deposition onto the membrane surface: Any presence of fouling will reduce the effective roughness of the membrane especially for the samples collected after long-term field operation.

The objectives of the first series of the analysis, referred as Analytical part I, were to:
- Observe changes in the membrane surface structure and describe the membrane morphology, for samples collected before and after long-term process operation
- Measure the membrane layers thicknesses from cross-section images
- Correlate these characteristics to changes observed in the operational behavior of the elements

The analytical techniques applied for these purposes were atomic force microscopy (AFM), scanning electron microscopy (SEM) and environmental scanning electron microscopy (ESEM) coupled with X-ray energy dispersive system (EDS).

2.1.1 Samples

Three SWRO membranes provided by Dow FILMTEC™[4] (Minneapolis, MN) were studied membrane A, B and C [7]. In a spiral wound module configuration they can appear with 400 ft^2 (37 m^2) and/or 440 ft^2 (40 m^2) of active membrane area. Membrane A is the highest rejection membrane with highest energy requirements for operation from this group of three. On the other hand membrane C is a low energy membrane with the highest permeate flow rate.

---

[4] ™Trademark of The Dow Chemical Company ("Dow") or an affiliated company of Dow

Figure 2.1 gives the water (A-value) and salt as NaCl (B-value) permeabilities of these membranes:
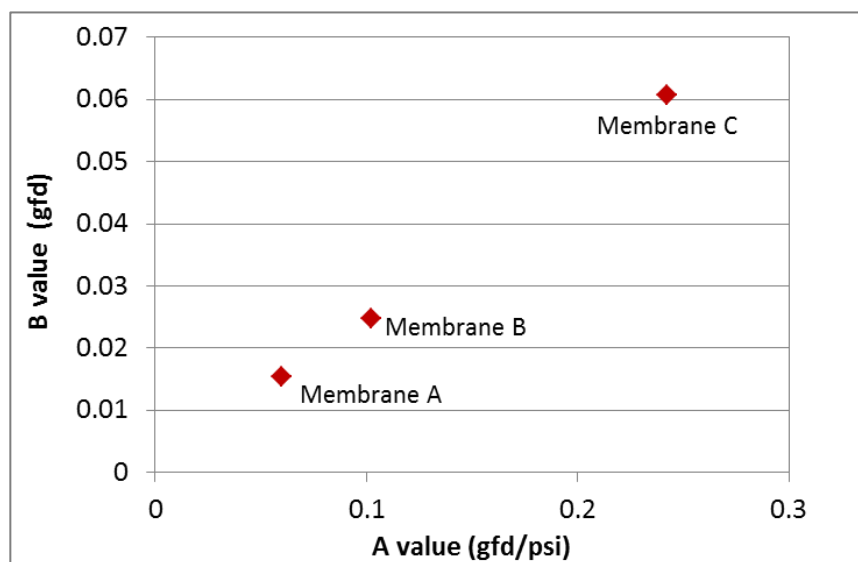
Figure 2.1. Salt passage (B-value) versus water permeability (A-value) for Dow FILMTEC™ SWRO membranes

In this study the samples collected for the analysis were split in three groups depending of their operation history:

1) Flat sheet membrane coming from a dry manufacturing roll - These are the reference samples in every analysis. They have never been in operation.
2) Flat sheet membrane taken from a manufactured element – These membranes have been through a wet standard test (55 bar feed pressure at 25 °C for a short period of time dictated by the manufacturer) in the manufacturing site and were subsequently stored wet in a preservative solution provided by the manufacturer. Samples from this group were only included in the series of analysis from Analytical part II (i.e., Chapter 3).
3) For Analytical part I samples were taken from manufacturing roll and operated at 15 bar and 25°C on a flat cell bench.
4) Samples collected from an element that was in long-term operation with synthetic or real seawater in a RO pilot plant.

Table 2.1 summarizes the operating condition and the exposure time of each. To help mitigate problems with the fouling all samples analyzed in this part were previously cleaned in the laboratory with 0.1%w NaOH and 0.2%w HCl in separated cycles and rinsed with ultrapure water.

Table 2.1. Samples list and operating history

	Serial Number [Year of the roll]	Element	Location	Max Operating Conditions	Exposure Time	Total Time in Operation	Analytical Phase I and II
1	F9159036	C-440	Element	25˚C 55 bar	20-30min	N/A	AP II
2	F9483359	A-400i	Element	25˚C 55 bar	20-30min	N/A	AP II
3	F9267337	B-440	Element	25˚C 55 bar	20-30min	N/A	AP II
4	[2015]	C	Flat Cell Bench	25˚C 15 bar	20-30min	N/A	AP I
5	[2015]	A	Flat Cell Bench	25˚C 15 bar	20-30min	N/A	AP I
6	[2015]	B	Flat Cell Bench	25˚C 15 bar	20-30min	N/A	AP I
7	[2015]	C	Roll	None	N/A	N/A	AP I and II
8	[2015]	A	Roll	None	N/A	N/A	AP I and II
9	[2015]	B	Roll	None	N/A	N/A	AP I and II
10	F9483392	A-400i	Pilot Plant	40˚C 75 bar	4-6 days	2 months	AP I and II
11	F9267299	B-400	Pilot Plant	40˚C 71 bar	4-6 days	2 months	AP I and II
12	F7701711	C-440	Pilot Plant	40˚C 66 bar	4-6 days	2 months	AP I and II
13	F7649967	C-440	Pilot Plant	45˚C 82 bar	6 days	6 days	AP I and II
14	F6289331	C-440	Pilot Plant	45˚C 45 bar	5 hours	5 hours	AP I and II
15	F7274977	C-440	Pilot Plant	45˚C 82 bar	< 5 hours	< 5 hours	AP I and II
16	F7274980	C-440	Pilot Plant	45˚C 82 bar	< 5 hours	< 5 hours	AP I
17	F7700904	A-400i	Pilot Plant	40˚C 75 bar	4-6 days	2 months	AP I
18	F9279785	A-440	Pilot Plant	43˚C 70 bar	2 months	2 months	AP II

49

2.2 Methodology

2.2.1 Method for AFM analyses

The AFM model utilized was Kaysight 5500 Atomic Force Microscopy N9410S available in SRCiT (Servei de Recursos Científics i Tècnics) at URV. Scanning was done in non-contact (tapping) mode. The unit is equipped with rotated monolithic silicon probe with chip size dimension 3.4 x 1.6 x 0.3 mm. The resonant frequency is 300 kHz, force constant of 40 N/m and speed of the scan 1 Hz. The images were analyzed using the WSxM software 5.0 developed by Nanotec Electronica S.L. (Spain) [8].

Differences in the membrane surface morphology can be expressed in terms of:

Average roughness (R_{avg}) – is defined as the average deviation from peaks and valleys from a mean plane. It shows how much rough the sample is. It is given by the following expression [2]:

$$R_{avg} = 1/S \int_0^a \int_0^b |f(x,y) - z_0| \, dxdy \qquad (2.1)$$

where S is the specific area, $f(x,y)$ is the height in the specific area, a and b are the length of two sides of the area, and Z_0 is the mean height. Z_0 is given by the following equation:

$$z_0 = 1/S \int_0^a \int_0^b f(x,y) \, dxdy \qquad (2.2)$$

Root mean square roughness (R_{rms}) - is the deviation of peaks and valleys from the mean plane. This number varies with the interval range. The R_{rms} is defined as:

$$R_{rms} = \left[1/S \int_0^a \int_0^b \{f(x,y) - z_0\}^2 \, dxdy \right]^{1/2} \qquad (2.3)$$

Five measurements on different positions were taken from every sample, each with specific area of 5 µm x 5 µm. Results for the average and root mean square roughness were generated using the software program. Furthermore the maximum and minimum values obtained in each series were discarded in order to statistically narrow the results variability. The mean was calculated from the remaining three values per series and those values were presented in the summary plot (Figure 2.4).

2.2.2   Method for SEM/ESEM analyses

The SEM model was JSM-6400 Scanning microscopy. The selected working distance was between 6-13 mm and beam voltage from 15kV to 20kV. Images with magnification of 500x, 5,000x and 25,000x were taken from the top, bottom surface and cross section of the membrane sample. Those samples analyzed with ESEM+EDS were not covered with gold. The measurements were done using the ImageJ software [9].

2.3 Results and discussion

2.3.1 AFM results

AFM topography images offer two dimensional views of the surface shape and profile. As seen in the images (Figure 2.2) the membrane surfaces are uneven and typically known as ridge-and-valley morphology. The phase imaging goes beyond simple topographical mapping to detect variations in composition, adhesion, friction and viscoelasticity. Applications include identification of contaminant, mapping of different components in composite, materials and differentiating regions of high and low surface adhesion and hardness [10]. As seen here the phase image is quite different for membrane A comparing to B and C and can be attributed to the specific differences in manufacturing. The selected amplitude tells the magnitude of the force applied on the surface when the tip hits it. The amplitude retrace represents the error retrace signal, i.e. error of the measurements.
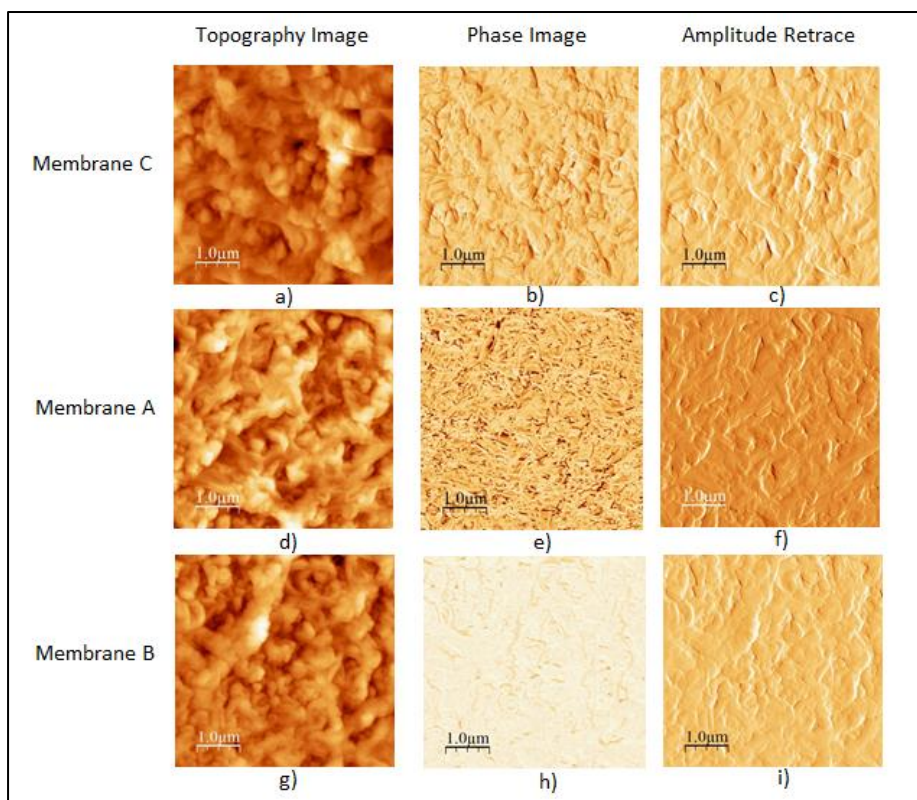
Figure 2.2. AFM images from samples from a roll (C, A and B – samples 7, 8 and 9 from Table 2.1)

Using the software we can create 3D image of the surface morphology. Figure 2.3 shows the 3D view of the membrane A taken from a roll (a) and sample collected after operation (b). It can be noticed lower sharpness of the hilltops and more smooth ridges of the ridge-and-valley structure for the samples that have been in operation. Because these images are not from the exact same sample quantitative conclusions (like difference in Z-axis) might be misleading and not fully accurate.
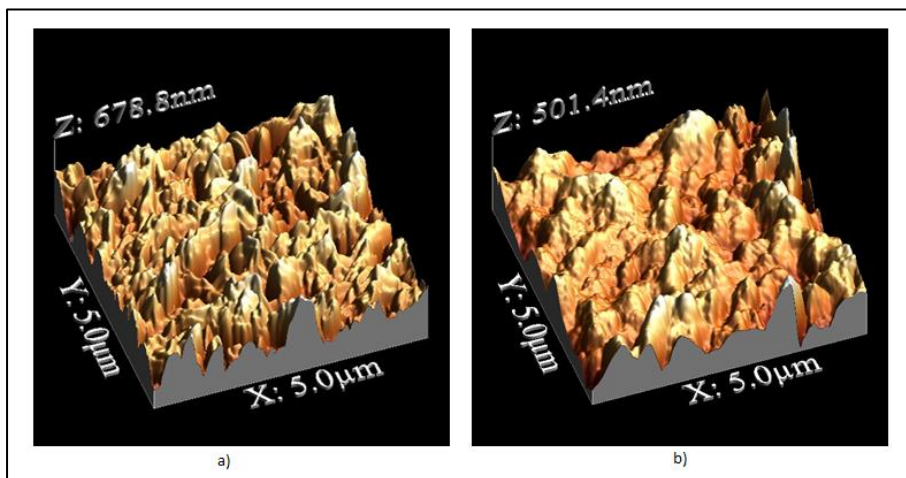
Figure 2.3. 3D image of the membrane surface a) membrane A roll b) membrane A F9483392 after operation

The summarized results from the analysis of the average and RMS surface roughness are presented in Figure 2.4. Two main conclusions can be drawn: (i) no linear relationship is observed between membrane surface roughness and permeability, per membrane type and (ii) the membrane surface roughness shows decreasing trend in the membrane after operation. Knowing that the permeability rate increases in the order A < B < C if linear relationship existed we should see the same trend in the increase of the surface roughness, which was not the case here. On the other hand we can see a 10-20% decrease in the surface roughness in the samples tested on a flat cell bench and almost 40% decrease for the compacted samples (for instance membrane C 967 that was operating on 45°C and 82 bar, sample 13 from Table 2.1).
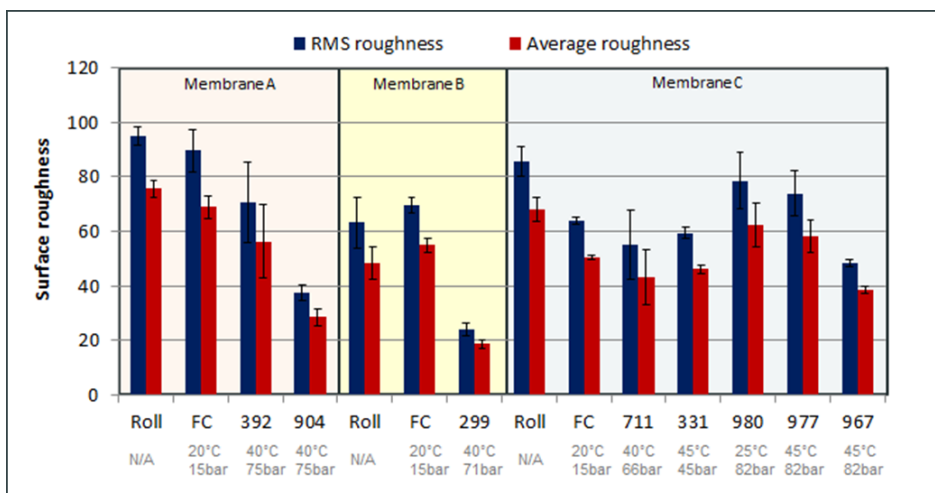
Figure 2.4. RMS roughness and average surface roughness for series of studied membranes (error bars are standard deviation)

2.3.2 SEM/ESEM results

Additional complementary insight in the membrane surface structure was obtained via SEM images. Figure 2.5 shows images for the surface and bottom side of membrane C with different magnification. This sample was collected from a manufacturing roll that had never been in operation. The top polyamide layer can be clearly observed on Figure 2.5c. It has an irregular and uneven surface visible with scale of 2 μm. On contrary the polyester fibers on the bottom side (Figure 2.5d) have massive structure seen already on 100 μm. With further zoom we can only see smooth and unwrinkled surface (Figure 2.5f). The top and bottom side of the membrane were also observed after two months in operation (Figure 2.6). The polyamide looks relatively similar to the roll sample. It was interesting to notice the dense polysulfone layer was penetrating through the polyester fibers. This may be a consequence of the pressure applied on the membrane. There are several possible implications of the water flow through this particular state of the membrane. The role of polysulfone and polyester layer is to provide the mechanical support to the active layer. As previously mentioned, the polyamide layer is primarily responsible for dictating the permeability and salt rejection of the composite membrane. But now in this situation the water pathway though the lower membrane layers is very likely obstructed compared to the state of the membrane given in Figure 2.5 when there are voids so the water can pass freely. The concept of the water transport now is changed because portion of those voids are occupied with dense polysulfone matter. Further experiments

54

and computational model analysis are needed in order to quantify the rate of water restricted per unit of area.
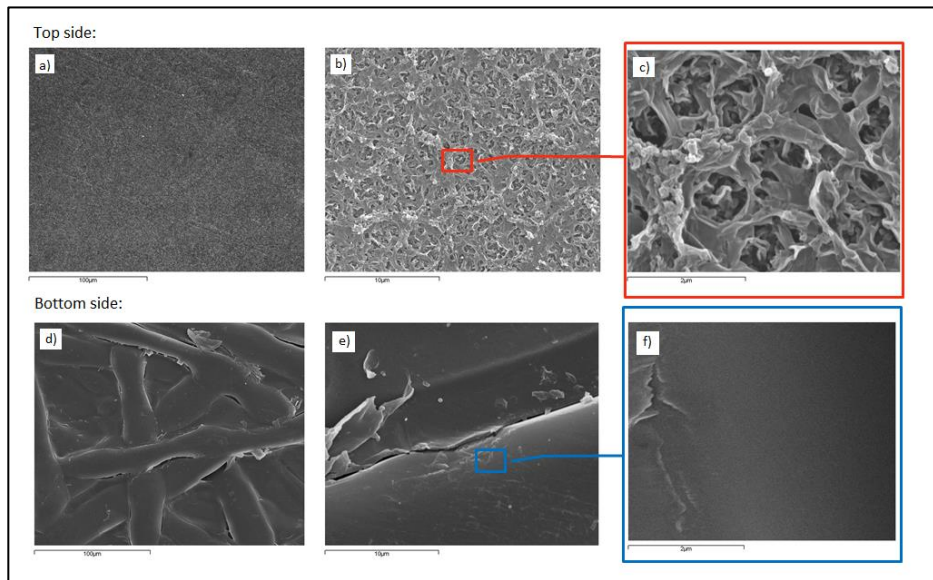
Figure 2.5. SEM images for the top and the bottom side of membrane C from a roll
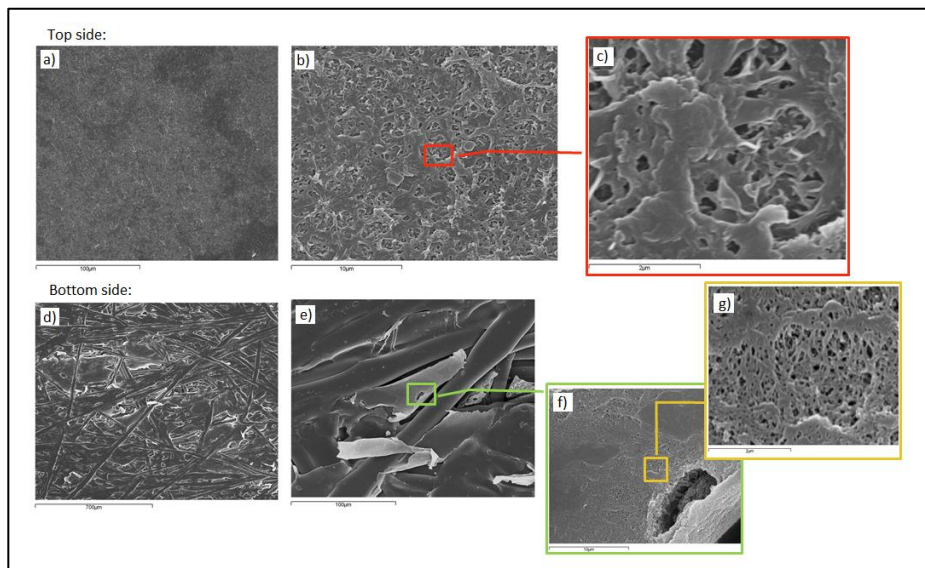
Figure 2.6. SEM images for the top and bottom side of membrane C F7701711 with different magnification

Another confirmation about the compression and penetration of the polysulfone layer was observed in membrane C after six days of operation at 45°C and 82 bar (with 64,062 mg/L as feed TDS). In Figure 2.7b we can clearly differentiate between the bottom side of the membrane, the poyester fibers and the polysulfone material (similar to previous Figure 2.6e).
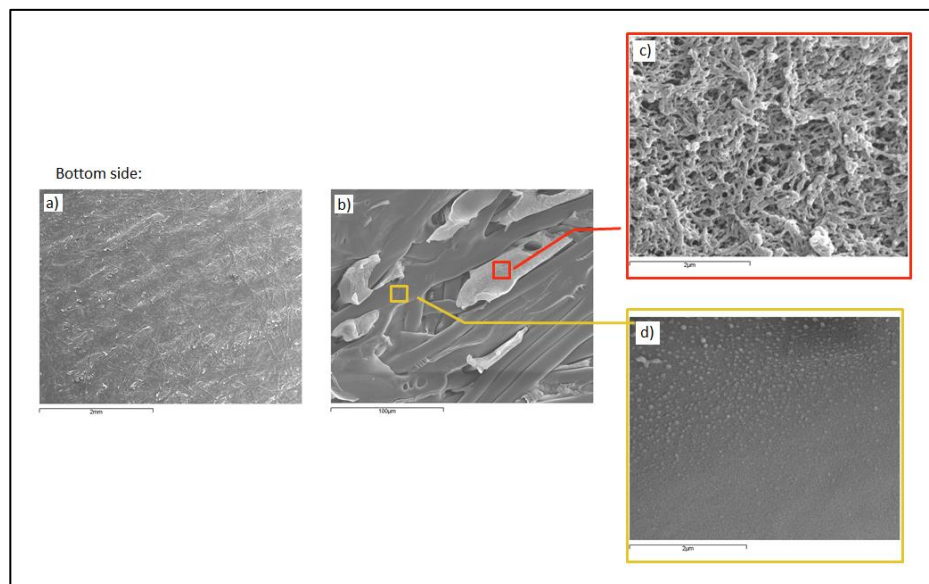
Figure 2.7. SEM images for the top and bottom side of membrane C F7649967 with different magnification

Another sample from membrane C F7649967 was used to take ESEM images and simultaneously run EDS analysis. Figure 2.8 gives the place selected on the membrane bottom to run EDS analysis and the spectra of the corresponding results. The identification of the sulfur element in the spectra of Figure 2.8a confirms that the brighter matter seen on the image is truly the polysulone layer.

In addition to the top and bottom, cross-section images of the membrane were collected with objective to observe if there are any changes in the membrane thickness. Samples for membrane C from roll, operated in flat scale bench and from element after operation in large pilot plant were utilized for the purpose (Figure 2.9a, b and c respectively).

Then different spot on each image were collected separately to measure (i) the polyamide plus plysulfone layer, (ii) the polyester layer and (iii) total thickness of the membrane. It was very difficult to measure and see the thicknesses of the polyamide layer alone so it was decided to take polyamide together with the polysulfone.
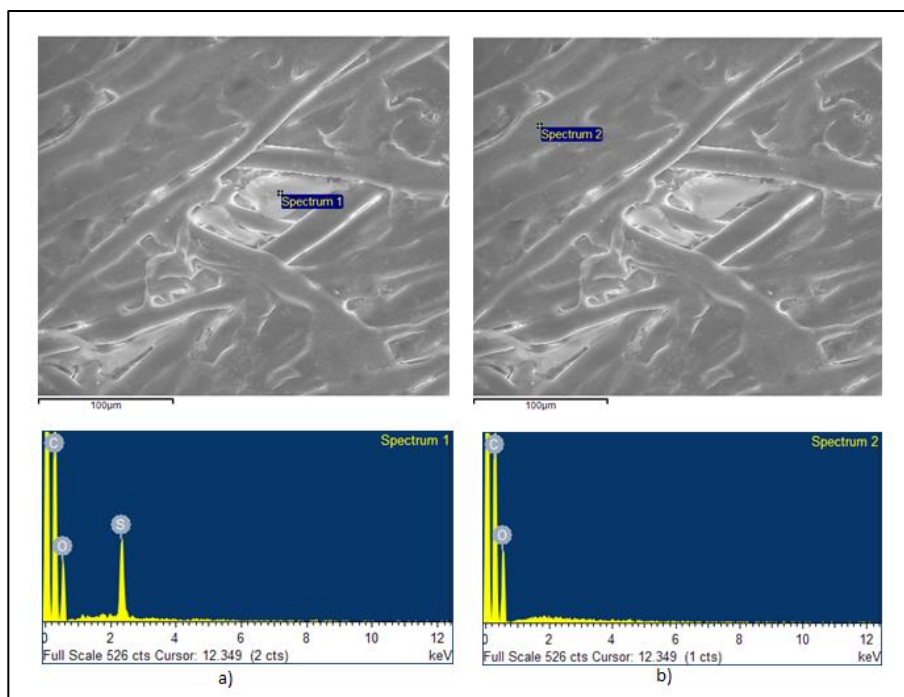
Figure 2.8. ESEM image with EDS analysis of the bottom of membrane C F7649967 a) Sulfur detected in the light part b) No presentence of sulfur in the areas appearing darker on the image
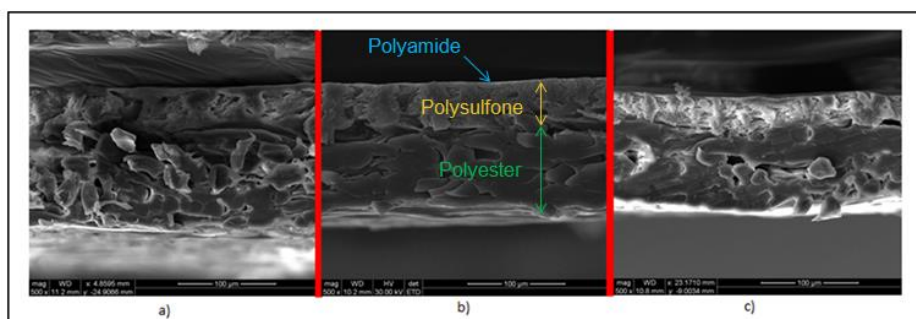
Figure 2.9. SEM cross-section images for membrane C a) Sample from a roll b) Sample operated on a flat cell bench c) Sample after long-term operation

From the summary we can see that the PA+PS layer did not suffer thickness reduction in the sample coming from the flat cell bench, but the polyester did (Figure 2.10). After the long term operation both PA+PS and polyester layer suffer reduction and therefore the total membrane thickness was reduced. In numbers the total membrane thickness was reduced by 33.50 µm (23% of the initial thicknesses of the roll sample) from which 21.55 µm or 14.8% belongs to

the polyester web layer and 11.95 µm or 8.2% to the PA+PS layer. The JMP analysis shows that those differences are statistically significant.
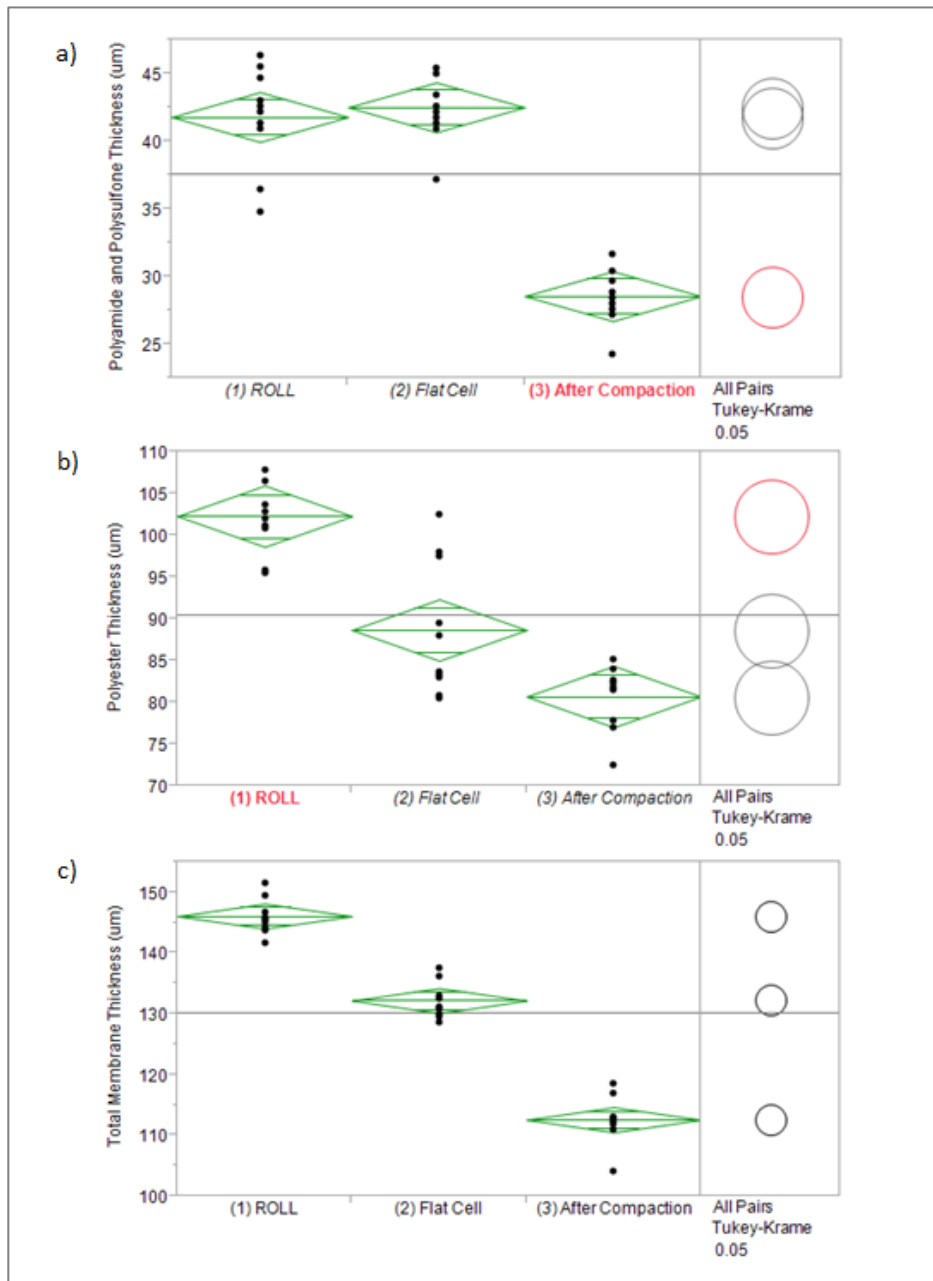
Figure 2.10. Membrane layer thicknesses a) Thicknesses of the polyamide & polysufone layer b) Thicknesses of the polyester layer c) Total membrane thickness

2.4   References

[1]. Tang, C.Y., Kwon, Y-.N., Leckie J.O. (2007) Probing the nano- and micro-scales of reverse osmosis membranes- a comprehensive characterization of physiochemical properties of uncoated and coated membranes by XPS, TEM, ATR-FTIR, and streaming potential measurements. *Journal of Membrane Science* 287, (1), 146-156.

[2]. Al-Jeshi, S., Neville A., (2006) An investigation into the relationship between flux and roughness on RO membranes using scanning probe microscopy. *Desalination* 189, 221-228.

[3]. Hirose, M., Ito, H., Kamiyama Y. (1996) Effect of the skin layer surface structures on the flux behaviour of RO membranes. *Journal of Membrane Science 121*, 209-215.

[4]. Kwak, S-.Y., Ihm, D. W. (1999) Use of atomic force microscopy and solid-state NMR spectroscopy to characterize structure-property performance correlation in high-flux reverse osmosis (RO) membranes. *Journal of Membrane Science* 158, 143-153.

[5]. Madaeni, S.S. (2001) The effect of surface characteristics on RO membrane performance. *Desalination* 139, 371.

[6]. Ghosh, A.K., Jeong, B-.H., Huang, X., Hoek, (2008) Impacts of reaction and curing conditions on polyamide composite reverse osmosis membrane properties. *Journal of Membrane Science* 311, 34-45.

[7]. The Dow Chemical Company, Midland, 2016. Available from: http://www.dow.com/en-us/water-and-process-solutions/products

[8]. WSxM Solutions, Nanotec Electronica. Available from: http://www.wsxmsolutions.com.

[9]. Image Processing and Analysis in Java. ImageJ. Available from: http://imagej.nih.gov/ij/index.html.

[10]. Phase Imaging: Beyound Topography, University of Guelph. Available from: http://www.chemistry.uoguelph.ca/educmat/chm729/afm/moredet.htm.

3 Chapter 3

This chapter provides a collection of results gathered together in order to give a description as complete as possible for the state of the polyamide layer after the process operation. The chemical composition of the polyamide and its characteristics were in the focus of the different analytical techniques employed.

3.1 Analytical Part II – Chemical characterization of the polyamide layer

Characterization of RO membranes is important since this allows an insight into the relationship between membrane chemistry, structure and transport properties. The most widely used characterization method is the measurement of the water flux and solute (usually NaCl) rejection for the membrane; these can be easily measured and so give a quick indication of the suitability of particular membrane for certain application. However fluxes provide only limited information about the characteristics and structure of the membrane and the role these play in water and solute transport. As a result, other characterization techniques are employed in order to determine parameters such as membrane elemental composition, ratio between selected functional groups, barrier layer thickness, its charge and open voids size [1].

The objective of the second series of analysis, referred as Analytical part II, was to provide complete characterization of the membrane chemical content before and after process operation (post compaction).

3.1.1 Formation of the polyamide layer

The selective polyamide barrier layer is formed *in situ* by polycondensation reaction of polyfunctional amine and acid chloride monomers at the interface of two immiscible solvents (Figure 3.1). In forming a polyamide thin film, a polyfunctional amine (MPD) is dissolved in water and a polyfunctional acide chloride (TMC) is dissolved in a polar organic solvent like Isopar L, hexane, cyclohexane, freon or isoparaffine [2,3,4]. The polymer is formed when the two monomer solutions are brought into contact at the liquid-liquid interface. The polymerization occurs predominantly in the organic phase [5,6,7]. Therefore is common to use a large excess of amine over acid chloride (typically about 20:1), which drives partitioning and diffusion of the amine into the organic phase. Different factors may influence on the solubility and diffusivity of the amine monomer in the organic phase which affects the reaction rate, and consequently, the morphology and structure of the resulting polyamide film, which ultimately define separation performance and interfacial properties [4,8]. Solvent properties and reaction conditions (particularly temperature) affect the density, viscosity, and surface tension of the organic solvent. The solvent surface tension controls amine solubility and, as a consequence, the amine-to-acid chloride concentration ratio in the reaction

zone and the degree of polymerization [9]. It is a very common practice to use combination of additives to influence monomer solubility, diffusivity, hydrolysis, or protonation or to scavenge inhibitory reaction byproducts [9].

Most studies of the MPD-TMC system indicate that curing is a necessary step to stabilize polyamide thin films [10,11]. Heat curing is used after film formation to remove residual organic solvent from the film and to promote additional crosslinking through dehydration of amine and carboxylic acid residues. This tends to increase water flux and salt rejection. With further increase in curing time or temperature the porosity of the polyamide film is reduced by crosslinking. This is accompanied by significant decrease in water flux, but increase in the salt rejection. However, exposure to high curing temperatures or long curing times can damage the microporous skin layer of the support membrane, which tends to decrease both water flux and salt rejection. Generally, curing temperatures ranging from 40 to 120°C are used [12].
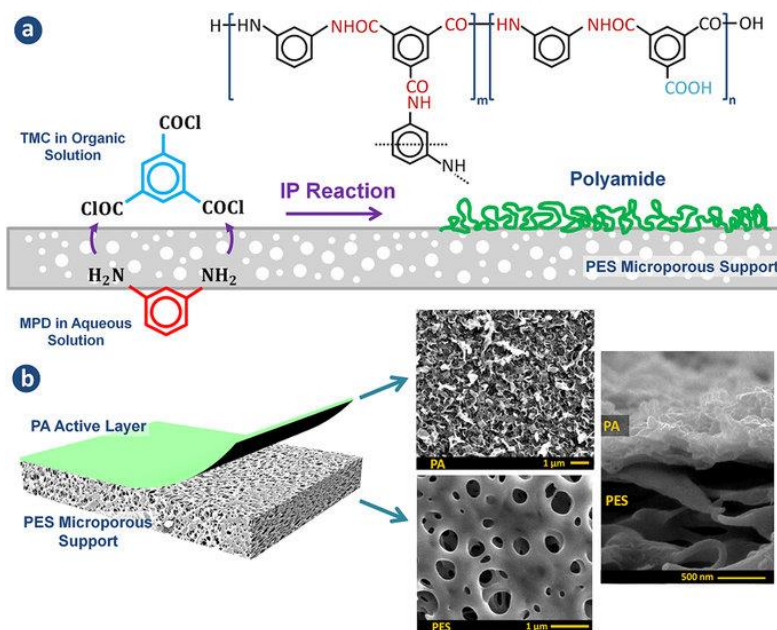
Figure 3.1. a) Schematic representation of the interfacial polymerization reaction between MPD and TMC at the surface of the microporous PES support and the chemical formula of PA layer. The m and n in polymer structure represents the crosslinked and the linear parts, respectively. b) Structure of the synthesized TFC membranes with the top and cross-sectional morphologies [13]

3.1.2 The swelling phenomenon

"Swelling is the process of dissolution of a polymer in a definite solvent" [15]. Initially, the solvent molecules slowly diffuse into the polymer to produce a swollen gel. When the polymer-polymer intermolecular forces are high, thanks to crosslinking, crystallinity, or strong hydrogen bonding only a swollen gel will be produced. On the other side, in presence of strong polymer-solvent interactions, the intermolecular forces might be overcome and, a second stage, the dissolution of the polymer may occur [14,15].

"The process of swelling results from the balance between repulsive and attractive phenomena. These phenomena may include: the thermodynamic mixing between the net polymer and the solvent; the interaction between fixed charged groups and free ions as happens in proton-exchange membranes; the elastic force of the polymer and also inter chain attractive forces" [15].

In the literature, membrane swelling has been described from two different perspectives: "macroscopic swelling" (or "bulk swelling"), which is defined as a large scale expansion of polymer membranes measured over an area of at least 1 mm^2, and "microscopic swelling", where the change in dimension is inferred from small-angle X-ray scattering (SAXS) data. The microscopic swelling observation is defined as the increase in the equivalent Bragg spacing as a results of solvation [15,16,17].

3.2 Methodology

Variety of analysis that combine more than one analytical technique were applied in order to characterize more profound the polyamide chemical content after compaction. Some of the methods are already known by the public scientific community (XPS, FTIR). Others were developed and conducted by the Analytical Science (Midland, USA) group in the Dow Chemical Company. Those analyses use proprietary, unpublished experimental methods and for the sake of confidentiality have been omitted from this version of the thesis.

3.2.1   XPS for studying the surface chemistry of polymers

X-Ray Photoelectron Spectroscopy (XPS) analysis, also known as Electron Spectroscopy for Chemical Analysis (ESCA), is a surface analysis technique that provides elemental and binding energy information about a material's surfaces and interfaces. This surface analysis technique utilizes an x-ray beam to excite the molecules on the surface of a solid material, resulting in the emission of photoelectrons. An energy analysis of these photoelectrons provides both elemental and chemical bonding information about a sample surface.

High resolution multiplex scan - measures the atomic concentrations of the elements identified in the survey scan (H and He cannot be detected). Detection limits are approximately 0.1 atom percent for most elements. Also it measures the chemical environment of each element through its binding energies. Precise determination of binding energies is made through the use of curve-fitting routines. A NIST (The National Institute of Standards and Technology is an agency of the U.S Department of Commerce) database is available for identifying binding energies with actual compounds.

The XPS data were acquired from an analyzed area having a diameter of 1 mm using a monochromatic Al Kα x-ray source. Low energy resolution survey scans were obtained from each membrane to determine what elements were present. The atomic concentrations of these elements and their local chemistries were determined from higher energy resolution multiplex scans.

This analysis in particular was conducted by the Innovatech Labs LLC (Plymouth, Minnesota) [18].

3.2.2   FTIR for studying the functional groups in the polyamide layer

Fourier Transform Infrared Spectroscopy (FTIR) is an analytical technique widely used in organic synthesis, polymer science, petrochemical engineering, pharmaceutical industry and food analysis. In 1989, Bartels examined RO membranes using infrared spectroscopy and he found that FTIR provided information on the functional groups, such as carboxylic acid or amide groups present in the composite membranes. Arthur made similar studies with several different composite RO membranes, and Avlonitis et al. in 1992 studied changes in aromatic polyamide membranes caused by chlorine degradation by following changes in the membranes spectra [1].

In our case the FTIR technique was applied for two different objectives, but only one is given in this version of the thesis:

FTIR to confirm the presence of the polyamide layer and evaluate its state in the membranes collected after operation. If the polyamide is not degraded due to oxidation during the process we should see the four characteristic peaks presented in the spectra at wavelength of 1663 cm^{-1}, 1608 cm^{-1}, 1545 cm^{-1} and 1446 cm^{-1}. The polysulfone peaks will be also present in the spectra at wavelength of 1586 cm^{-1}, 1505 cm^{-1} and 1489 cm^{-1}. The spectra of the samples are always compared with the spectra of reference, fresh membrane that was not used in operation.

The samples in this case were taken directly from element after autopsy and they hold all the layers of the composite. The general conditions of the measurements were: 100 scans, 8 resolution, Ge crystal, range of 600-4000 cm^{-1} and gain at 1. The instrument used was iZ10 Fourier Transform Infrared Spectroscopy with Attenuated Total Reflectance (FTIR-ATR), from Thermo Fisher Scientific.

3.3   Results and discussion

3.3.1   XPS results

In the element surface analyses the following atoms were included: carbon (C), chlorine (Cl), nitrogen (N), oxygen (O) and sulfur (S). Table 3.1 below gives the atomic concentration (expressed in percentage) for the control and the membrane sample. The analysis for chlorine was included in order to check the presence of an oxidizing agent that might be an indication for potential chlorination of the element during the operation and degradation of the polyamide layer [19]. Because no change in the binding energy (196-199 eV) was noticed for chlorine between the samples, the option of membrane chlorination was discarded. The concentration of sulfur is fairly low and thus will be not considered for further evaluation. Regarding the C, N and O, there is evident change in their atomic concentrations between the control and the samples.

Table 3.1. Relative atomic concentration of the elements analyzed by XPS

Atomic concentration	C (%)	Cl (%)	N (%)	O (%)	S (%)
Control A	75.6	N/A	11.8	12.3	0.2
Compacted A	70.7	N/A	10.8	18.1	0.4
Control B	75.3	0.1	11.2	13.2	0.2
Compacted B	69.2	0.1	10.3	20.2	0.2
Control C	76.2	0.1	11.3	12.2	0.2
Compacted C	69.4	0.2	10.4	19.7	0.3

In the literature [13,20,21] a method is reported that gives correlation between the O/N ratio and the degree of cross-linking of the polyamide chain. According to the method, the theoretical O/N ratio is 1.0 when the PA layer is fully cross-linked (n=1) Table 3.2, i.e., all the O and N atoms are associated with the amide groups to give a 1:1 ratio. This ratio becomes 2:1 for the linear polyamide with no cross-linking (n=0). The theoretical elemental compositions are computed based on a polyamide layer formed by trimesoyl chloride and 1,3-benzendiamine. When n=1, the resulting polymer is fully cross-linked and every acid chloride monomer is linked with 1.5 amine monomers to give a molecular formula of C_6H_4ON. When n=0, the resulting polymer is linear and

every acid chloride monomer reacts with one-amine monomer to give a molecular formula of $C_{15}H_{10}O_4N_2$ [20].

Following this approach, the atomic composition of the control membranes (A, B and C) is similar to the theoretical values for fully cross-linked polyamide. On the other hand, the atomic composition of the samples is very similar to the theoretical values for the fully linear stucture of the polyamide (Figure 3.2).

Table 3.2. Theoretical values for the elemental composition and O/N ratios for TFC membranes

Theoretical values	C (%)	N (%)	O (%)	O/N ratio
Fully cross-linked	75.0	12.5	12.5	1.0
Fully linear	71.4	9.5	19.1	2.0

The Ratio O/N for the set of six samples is given on the plot below:
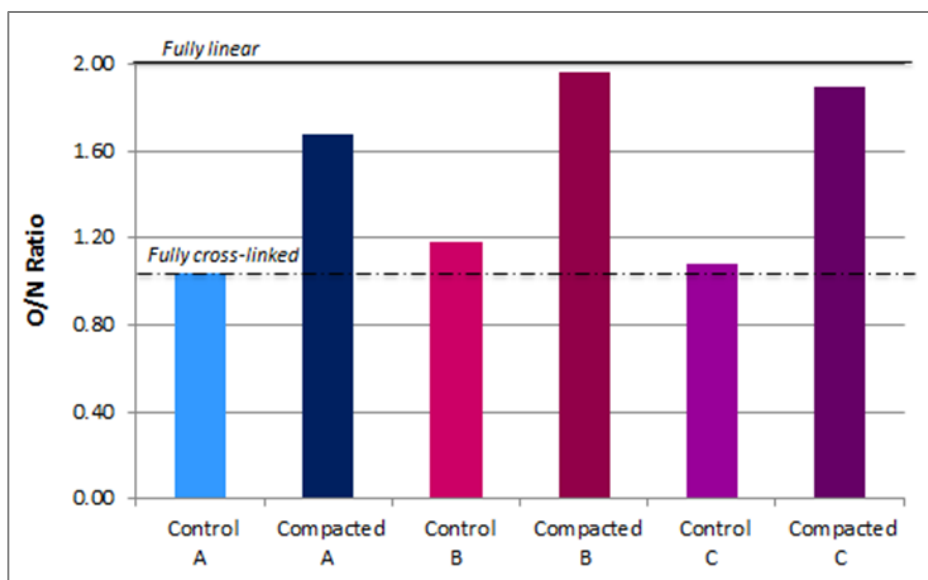
Figure 3.2. O/N ratio for the control and sample membranes

On the Table 3.2 above it can be noticed that atomic concentration of carbon decreased by ~5% in the membranes sample compared to their controls. In order to understand the reorganization of carbon within the polymeric chain

67

the binding energy was used to assign it to different functional groups. Below in Table 3.3 are given the binding energy ranges for the relevant functional groups (the assignments referring to the starred element in each bonded state) [22].

The carbon chemistry as percentage per groups is given in Figure 3.3 for the same set of six membranes. When comparing the control with the membrane sample it can be noticed that the C-C bonding rate shows decreasing trend, while the C-O or C-N and C=O or O=C-N show increasing bonding rates. These trends were comparable for the three membranes analyzed here A, B and C.

Table 3.3. Binding energy ranges for the relevant functional groups [23]

Binding Energy (eV)	Peak Assignments
285.0	$C-C^{\bullet}$
286.3-286.7	$C^{\bullet}-O, C^{\bullet}-N$
288.0-288.5	$C^{\bullet}=O, N-C^{\bullet}=O, N-C^{\bullet}=N, O-C^{\bullet}=N$
289.0	$O-C^{\bullet}=O$
530.9	$O^{\bullet}=C-N$
531.6-532.0	$O^{\bullet}=Si=O^{\bullet}$
532.2-532.5	$C=O^{\bullet}, S=O^{\bullet}$
533.2-533.7	$O=C-O^{\bullet}, C-O^{\bullet}-C, O^{\bullet}-SO_2$
398.7-399.3	$C=N^{\bullet}, C\equiv N^{\bullet}$
399.7-400.2	$C-N^{\bullet}, N^{\bullet}-C=O, C-N^{\bullet}=O$
401.2	$-N^{\bullet}H_3^{+}$
401.6	$-N^{\bullet}RH_2^{+}$
402.6	$-N^{\bullet}R_3^{+}$
169.7-169.9, 168.7-168.9	$O-S^{\bullet}O_2$
168.9-169.2, 167.7-168.0	$O=S^{\bullet}=O$
168.0, 167.1	$O=S^{\bullet}-NH_2$
167.1, 165.9	$S^{\bullet}-NH_2$
164.7, 165.9	$S^{\bullet}-CH_3$
164.9-165.1, 164.0-163.7	$S^{\bullet}$
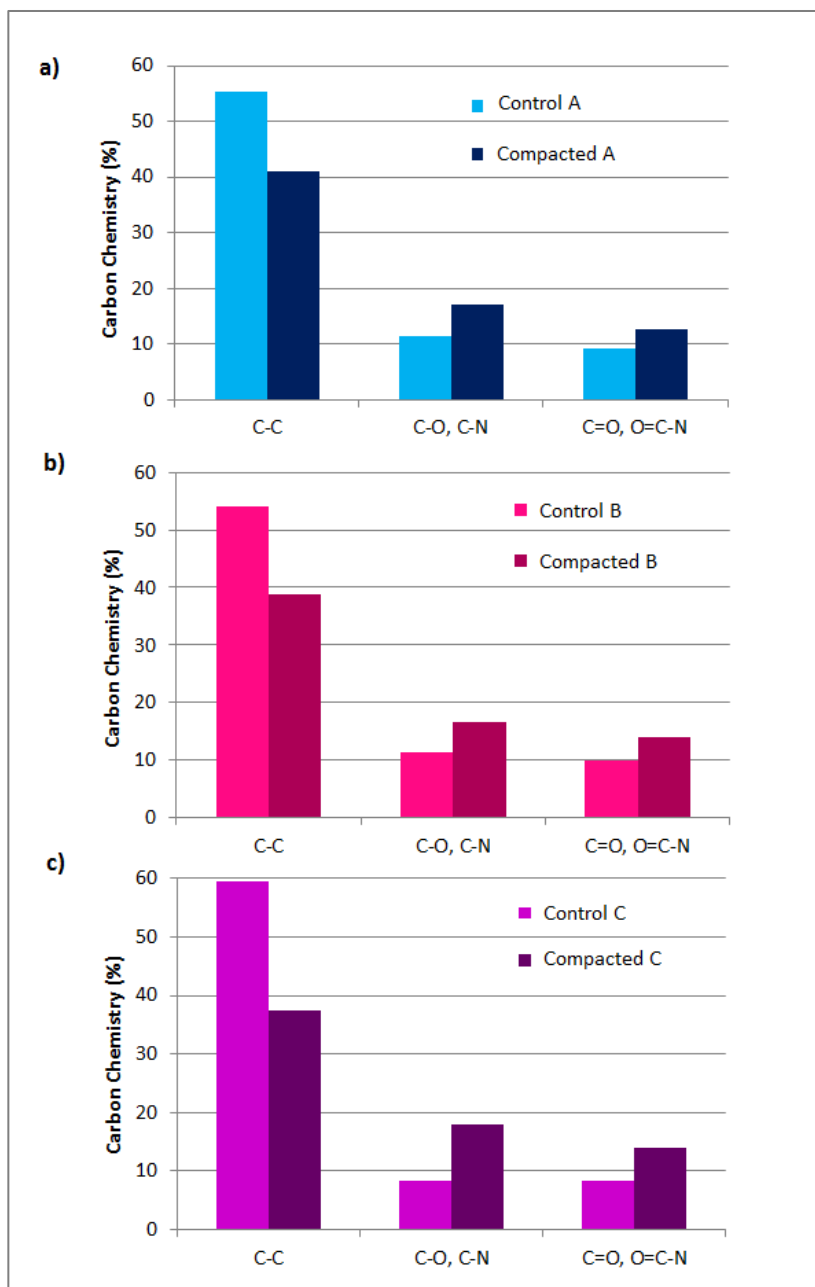
Figure 3.3. Carbon chemistry (relative percent) for the control and sample membrane a) A b) B c) C

3.3.2 FTIR results

The analysis on the polyamide peaks by FTIR for four samples (A F9483392 and 9279785, B F9267299 and C F7701711) are given in Figure 3.4. The four characteristic peaks coming from the polyamide are present which confirms that there is no degradation of the layer due to possible oxidation during the process operation or other chemical attack. The other membrane samples that were subject of analysis in this thesis and are not given here is because they are coming from the same trials as the four membrane selected above as representative.
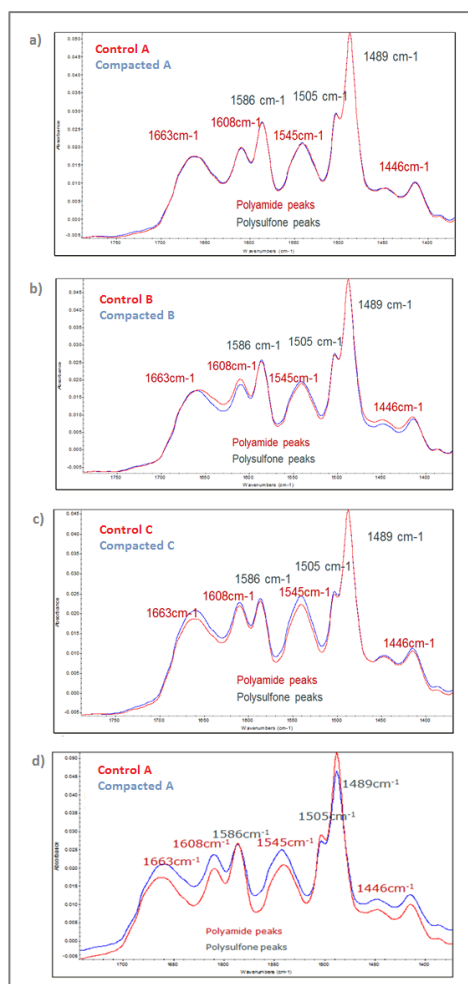
Figure 3.4. FTIR spectra with the polyamide and polysulfone peaks for pair of reference and case membrane a) A-F9483392 b) B-F9267299 c) C-F7701711 d) A-F9279785

3.4 References

[1]. Williams, M.E. (2003) A brief review of reverse osmosis membrane technology, white paper. EET Cprporation and Williams Engineering Services Company, Inc.

[2]. Chau, M.M., Light, W.G., Swamikannu, A.X. (1993) Chlorine-tolerant, thin-film composite membrane. US Patent 5,271,843.

[3]. Hachisuka, H. and Ikeda, K. (2002) Reverse osmosis composite membrane and reverse osmosis treatment method for water using the same. US Patent 6,413,425.

[4]. Verissimo, S., Peinemann, K.V. and Bordado, J. (2005) Thin-film composite hollow fiber membranes: an optimized manufacturing method. *Journal of Membrane Science* 264, 48-55.

[5]. Freger, V. (2005) Kinetics of film formation by interfacial polycondensation. *Langmur* 21, 1884-1894.

[6]. Morgan, P.W. (1965) Interfacial polimerization without stirring. In *Condensation Polymers; by Interfacial and Solution Methods* (pp. 19-64) Interscience Publishers, New York.

[7]. Morgan, P.W., Kwolek, S.L. (1996) Interfacial polycondensation II. Fundamentals of polymer formation at liquid interfaces. *Journal of Polymer Science* 34, 531-559.

[8]. Wittbecker, E.L., Morgan, P.W. (1996) Interfacial polycondensation 1. *Journal of Polymer Science* 34, 521-529.

[9]. Ghosh, A.K., Jeong, B-.H., Huang, X., Hoek, (2008) Impacts of reaction and curing conditions on polyamide composite reverse osmosis membrane properties. Journal of Membrane Science 311, 34-45.

[10]. Rao, A.P., Desai, N.V., Rangarajan, R., (1997) Interfacially synthesized thin film composite RO membranes for seawater desalination. *Journal of Membrane Science* 124, 263-272.

[11]. Rao, A.P., Joshi S.V., Trivendi, J.J., Devmurari, C.V., Shah V.J., (2003) Structure-performance correlation of polyamide thin film composite membranes:effect of coating conditions on film formation. *Journal of Membrane Science* 211, (1), 13-24.

[12]. Mickols, W.E. Composite membrane and method for making the same. US Patent 6,562,266.

[13]. Khorshidi, B., Thundat, T., Fleck B.A., Sadrzadeh, M. (2016) A novel approach toward fabrication of high performance thin film composite polyamide membranes. *Scientific Reports* 6, 22069; doi: 10.1038/srep22069.

[14]. Billmeyer, F.W. (1984) Textbook of Polymer Science. John Wiley & Sons, New York.

[15]. Izak, P., Hovorka, S., Bartovsky, T., Bartovska, L., Crespo J.G. (2007) Swelling of the polymeric membranes in room temperature ionic liquids. *Journal of Membrane Science* 296, 131-138.

[16]. Gebel, G. Structural evolution of water swollen perfluorosulfonated ionomers from dry membrane to solution. *Polymer* 41, 5829.

[17]. Fujimura, M., Hashimoto, T. and Kawai, H. (1982) Small-angle X-ray scattering study of perfluorosulfonated ionomers. *Macromolecules* 15, 136.

[18]. Inovatech Labs, LLC, Plymouth, MN.
http://www.innovatechlabs.com/analytical-services-esca-details.htm

[19]. Kwon Y., Leckie J.(2006) Hypochloride degradation of crosslinked polyamide membranes II. Changes in hydrogen bonding behavior and performance. *Journal of Membrane Science* 282, 456-464.

[20]. Tang, C.Y., Kwon, Y-.N., Leckie J.O. (2007) Probing the nano- and micro-scales of reverse osmosis membranes- a comprehensive characterization of physiochemical properties of uncoated and coated membranes by XPS, TEM, ATR-FTIR, and streaming potential measurements. *Journal of Membrane Science* 287, (1), 146-156.

[21]. Kim, S. H., Kwak, S-.Y., Suzuki, T. (2005) Positron annihilation spectroscopic evidence to demonstrate the flux-enhancement mechanism in morphology-controlled thin-film composite (TFC) membrane. *Environmental Science & Technology* 39, 1764-1770.

[22]. Subrahmanyan, S. (2003) An investigation of pore collapse in asimetric polysulfone membranes, PhD Thesis. Virginia Polytechnic Institute, Blacksburg, Virginia

4   Chapter 4

This chapter describes series of flat cell tests conducted in order to segregate the compaction flow loss between its constituents (polyamide and polysulfone) and determine if any sizeable portion of the total flow (under certain temperatures and pressure) is due to the polyamide compaction.

4.1   Analytical Part III – Flat cell testing

As previously discussed in the first chapter one of the main performance changes in RO due to compaction is the lower production rate. Moreover there is a portion of the flow loss that cannot be recovered after subsequent chemical cleanings. The major reason for this flow loss generally is attributed to the physical changes of the polysulfone layer (thinner, denser, etc.). However there are lack of experimental data that really shows how much of the flow loss is due to changes in the polyamide and how much is due to polysulfone compaction. In direction with the hypothesis stated in this research, the approach taken here considers that those changes are most probably physical and chemical for the polyamide and only physical for the polysulfone. And both of them contribute to the overall mechanical transport model. In order to draw solid conclusions regarding this question, series of flat cell tests were performed in order to segregate compaction flow loss between its constituents (polyamide and polysulfone) and determine if any sizeable portion of the total flow (under certain temperatures and pressure) is due to the polyamide compaction.

4.1.1   Samples preparation

The approach considered uses a composite sample which contains all the three layers and a sample that contain only the support layers, polysulfone and polyester. For that purpose, an oxidation agent (NaOCl) was used to remove the polyamide layer. Here are given the steps followed to prepare the membrane coupons for the testing:

2-days before the flat cell test

1. 24 coupons from membrane A were cut (1.5" x 5" rectangular) directly from the center of a membrane roll (later the number of repetitions was reduced by half for membrane B and C).
2. From those 24 coupons, 8 were selected for bleaching. The other 16 were left for soaking in a container of RO water.
3. Bleaching – Samples were soaked in 6% NaOCl solution at room temperature for ~18 hours.

1-day before the flat cell test

4. The following day, the 8 coupons were removed from the chemical solution. Then the samples were rinsed well with RO water and placed in a container of RO water for overnight soaking.

5. The water in the container was exchanged for fresh RO water at least twice during the day.

Day of the flat cell test

6. All 24 coupons were soaked in 35% Isopropyl alcohol (IPA)/water solution for one hour. In respect to the 8 coupons that were previously bleached it's very important to rinsed well and make sure that no bleach was leftover. This is very important step from safety perspective due to the reactive chemistry between NaOCl and Isopropyl alcohol that leads to creation of chloroform.

7. The coupons were removed from IPA/water solution, rinsed and soaked in RO water for additional hour.

8. Compaction tests were conducted as listed in table Figure 4.1.

4.2 Methodology

The intention with this pure water permeability (PWP) testing was to quantify the total (entire membrane) and the partial layer's (polyamide versus polysulfone) flow loss due to compaction for three different RO membrane types (A, B and C) from Dow FILMTEC™[5] SWRO portfolio. The range of temperature and pressure assessed was 15 to 45°C and 28 bar (400 psi) to 69 bar (1000 psi), respectively. Figure 4.1 depicts the samples arrangement per cell: in one cell was placed the composite sample (contains all membrane layers) and in other cell were placed the second composite (from the same membrane type) and the PS/PET support layer obtained after bleaching. The role of the composite membrane in the second cell is to add resistivity and balance the flow during the operation. As the PS/PET support has ~70 times higher permeability rate than the composite membrane this might cause problem in the operation and instrumentation of the flat cell bench. The main approximations taken by applying this method are (1) both composite membrane coupons perform equally and (2) there is no added compaction due to the pressing force in the second cell where two membrane coupons have been placed. The permeability obtained in the cell with the composite sample

---

[5] ™Trademark of The Dow Chemical Company ("Dow") or an affiliated company of Dow

was used to get the PS/PET permeability from the cell with the composite and bleached sample by subtracting it. As the test was including four to eight replicates, in the data analysis the average of all was used. The following equations were applied to get the polyamide and polysulfone permeability through its resistivity:

$$R_{single} = \frac{1}{A_{single}} \qquad (4.1)$$

$$R_{stacked} = \frac{1}{A_{stacked}} \qquad (4.2)$$

$$R_{PS} = R_{stacked} - R_{single} \qquad (4.3)$$

$$R_{polyamide} = R_{single} - R_{PS} \qquad (4.4)$$

$$A_{polyamide} = \frac{1}{R_{polyamide}} \qquad (4.5)$$

$$A_{PS} = \frac{1}{R_{PS}} \qquad (4.6)$$

where R_{single} is the resistivity of the composite sample, $R_{stacked}$ is the resistivity given by the composite and bleached sample altogether. $A_{polyamide}$ and A_{PS} are the permeabilities of the polyamide and support, respectively. Furthermore, a series resistance model equation was used that helps to determine the contribution of each layer to the final compaction behavior of the composite membrane i.e. the added resistance of the polyamide and polysulfone to the overall resistivity of the membrane:

$$\frac{1}{A_{composite}} = \frac{1}{A_{polyamide}} + \frac{1}{A_{PS}} \qquad (4.7)$$
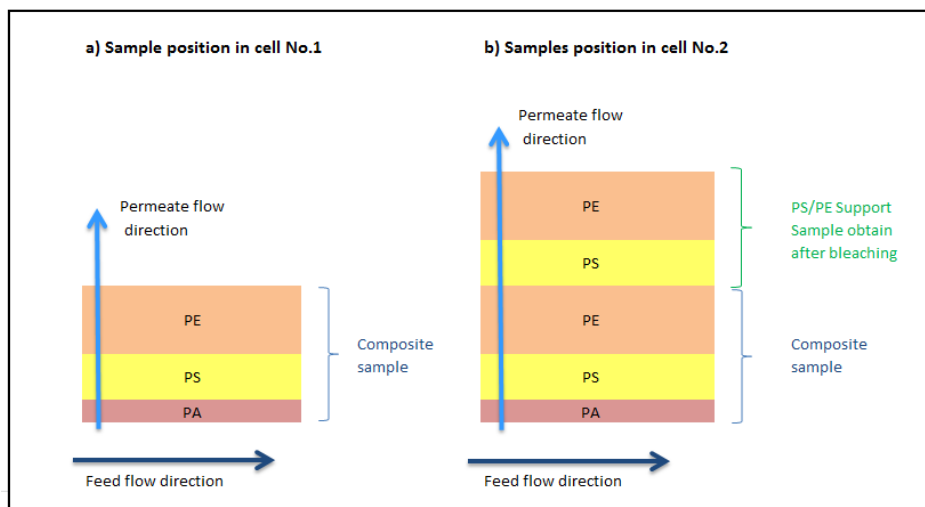
Figure 4.1. Sample arrangement in the cells

For the tests with membrane A were considered eight repetitions, and due to acceptable variation the repetitions were reduced to four for the B and C testing.

Table 4.1. List with the membrane types and conditions on which were tested

Test No.	Membrane	Number of coupons	Temperature (°C)	Pressure (bar)
1	A	24 in total (16 comosite + 8 bleached)	15	28, 55 and 69
2	A	24 in total (16 comosite + 8 bleached)	45	28, 55 and 69
3	B + C	24 in total (16 comosite + 8 bleached)	15	28, 55 and 69
4	B + C	24 in total (16 comosite + 8 bleached)	45	28, 55 and 69

The uncertainties that this method holds are:

- The bleaching part should be properly done to ensure no polyamide is left on the support coupon;
- The expected A-value of a composite membrane is around 0.85 lmh (0.5 gfd/psi) on standard conditions;
- The expected A-value of a PS support (uncompacted) is around 59.5 lmh (35 gfd/psi).

In this case additional verification was considered by having an extra coupon after bleaching to assess the permeability of the PS/PET support by itself in a separate low pressure (0.68-1.03 bar) water permeability cell.

Under general terms when the effective feed pressure increases, the permeate TDS will decrease while the permeate flux will increase when the other parameter (feed TDS, feed flow, temperature etc.) are kept constant as shown in Figure 4.2a. Other variable parameter that influences the flux and rejection of the membrane is the temperature. As Figure 4.2b demonstrates, membrane productivity is very sensitive to changes in feedwater temperature. When water temperature increases and all other parameters are kept constant, the permeate flux increases almost linearly due to the higher diffusion rate of the water through the membrane. Increased feed water temperature also results in lower salt rejection or higher salt passage. This is due to a higher diffusion rate for salt through the membrane. Water permeability (or A-value) on the other side will also show an increase with increase of the temperature.
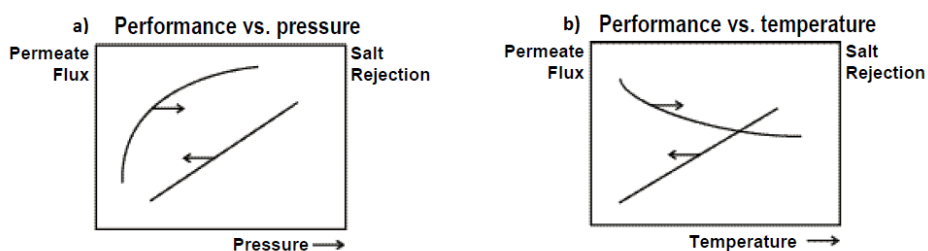
Figure 4.2. Impact of the pressure and temperature to the permeate flux and salt rejection [1]

The relationship between the flux and A-value in the absence of compaction is given with the following expression:

$$Flux \ (gpd) = A\big(f(T)\big) \cdot (P_{feed} - P_{permeate}) \qquad (4.8)$$

In theory, because the temperature is the only parameter that influences the permeability, when the feed pressure increases and the temperature is kept stable we should see no change in permeability rate of the given composite membrane. In reality, permeability decrease is observed and the reasons for that could be multiple. One of the main reason been referred is the polysulfone (support) compaction i.e physical changes of the polysulfone material.

The approach used to interpret the results of the testing described in this chapter is that in case of an ideal material is present (hypothetically to imagine a perfect material that suffers no changes, mechanically, physically, chemically or any similar) then we should see no changes in the water permeability. Thus

78

constant permeability is expected for layers which do not compact. In this particular case the permeability of both the polyamide and support in the first testing point at 28 bar was taken as their ideal case to quantify their permeability loss, separately. In fact this is already a semi-ideal case because we may have certain compaction on 28 bar, and depending of the range of temperature and pressure studied as well as the selection of the first point the outcome values will look differently. Furthermore the identified portions were reflected in the total permeability loss of the entire composite membrane. In such a way we can have a clear picture about the contributions of each layer into the total amount of flow loss.

4.3   Results and discussion

From the cells with the composite sample the total membrane flow loss was extracted for membrane A, B and C taking the test at 28 bar as reference. As shown in Table 4.2 the flow loss ranges 13-20% for A, 15-21% for B and 21-29% for C for temperature difference from 15°C to 45°C. Therefore this series suggest very clearly that (1) the flow loss is higher on higher temperature for the same membrane type and (2) compering this series of three, the most permeable membrane i.e. C shows the highest percentage of total flow loss, up to 29% for 69 bar and 45°C. Other information gathered form this testing were the polyamide and polysulfone flow loss considered individually. The polysulfone flow loss seen for A was 54-61% and 46-66% for C. In this evaluation in particular the test done with B on 15°C gives no logical values and will be neglected in this results discussion. Regarding the polyamide layer flow loss the observed range with the temperature and pressure increase was 4-11% for membrane A, 10-18% for B and 19-27% for C. The trends seen earlier for the total flow loss are also reflected here.

In order to complement the discussion, Figure 4.3 summarizes the support and polyamide water permeability for the three membrane types A, B and C. The dashed lines on these plots represent the expected permeability in ideal (absence of compaction) case taking the pressure of 28 bar (400 psi) as reference at each temperature. For a temperature of 45°C we can see that the PS/PET permeability loss at 69 bar (1000 psi) is 62% for A (Figure 4.3a), 56% for B (Figure 4.3c) and 66% for C (Figure 4.3e). In fact, because the support used to manufacture these three SWRO membranes is equal, the author expectations

79

was to get even more narrow distribution regarding the portion on flow loss seen in the polysulfone layer as a results of compaction. Meaning the flow loss seen in the polysulfone will be comparable for the three different membranes; while the flow loss of the polyamide will differ significantly due to the differences in the formation on those PA layers. Consequently, the PA layer flow loss will have its impact on the total membrane flow loss seen in the composite. This is a very general assumption that requires additional testing to be verified eventually. However even the initial permeability loss at 15°C for the support in relatively high, above 46%. In Figure 4.3 d the data point is missing for the PS/PET permeability rate on 15°C and 28 bar (400psi) due to an error of the measurement (a negative value was obtained and thus is not represented on the corresponding plot).

On the other side, the polyamide permeability flow loss at 15°C is minor for A, only 4% and slightly higher for B and C, 10% and 19% respectively (Figure 4.3b, d, f). With the temperature increase to 45°C those percentage enlarged compare to the ideal case to 12%, 18% and 27% accordingly. Being able to assess these percentage means that indeed there is sizable portion about the polyamide permeability decrease which is clear evidence of polyamide compaction as well. The interesting thing in this series is the trend indicating that more permeable membranes are probably more prone to compaction. Nevertheless, more systematic analysis is needed to confirm on that.

The question worth raising now is: what are the changes in the polyamide structure that leads to these permeability losses? Could be changes in the physical structure of the polyamide or as the main hypothesis and the analyses covered in chapter three aims, one possible reason investigated here was the change in the chemical content of the polyamide layer.

Table 4.2. Total membrane, PS/PET and PA layer flow loss for membrane A, B and C

Membrane A	Temp	28 to 55 bar (400 to 800 psi)	28 to 69 bar (400 to 1000 psi)
Total flow loss	15˚C	9.55%	13.42%
	45˚C	12.19%	20.07%
PS/PET flow loss	15˚C	43.34%	54.83%
	45˚C	53.89%	61.56%
PA flow loss	15˚C	3.50%	4.18%
	45˚C	4.57%	11.65%

Membrane B	Temp	28 to 55 bar (400 to 800 psi)	28 to 69 bar (400 to 1000 psi)
Total flow loss	15˚C	10.78%	15.39%
	45˚C	22.20%	21.81%
PS/PET flow loss	15˚C*	105.77%	104.07%
	45˚C	45.60%	56.13%
PA flow loss	15˚C	7.28%	10.94%
	45˚C	20.59%	18.81%

* The obtained values are not relevant, the test should be repeated

Membrane C	Temp	28 to 55 bar (400 to 800 psi)	28 to 69 bar (400 to 1000 psi)
Total flow loss	15˚C	14.08%	21.16%
	45˚C	27.90%	29.75%
PS/PET flow loss	15˚C	38.47%	46.61%
	45˚C	60.39%	66.16%
PA flow loss	15˚C	12.48%	19.39%
	45˚C	25.98%	27.29%
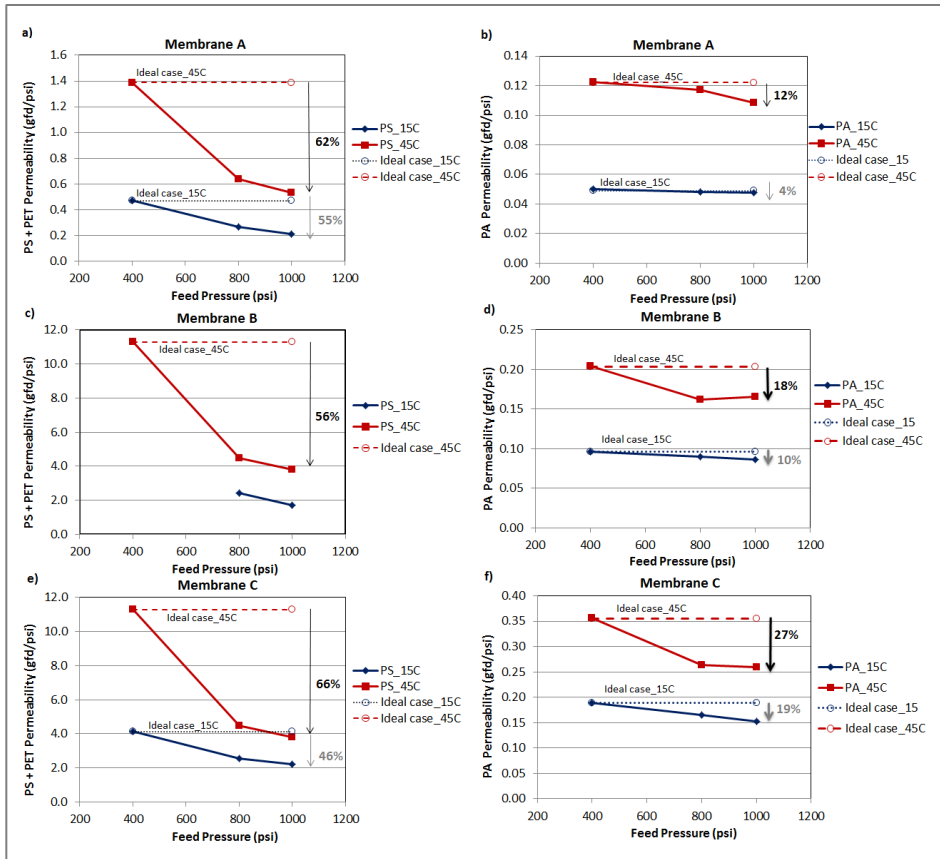
Figure 4.3. Polysulfone/polyester and polyamide permeability loss with temperature and pressure increase

Figure 4.4 gives the percentage of added resistance coming from the polyamide and support to the compacted composite membrane. The results indicate that the polyamide portion is contributing significantly in the case of elevated temperature i.e. 45°C. Moreover this portion is going bigger as the membrane is more permeable, up to 85% for C. However no change for C is noted with the temperature increase from 15°C to 45°C. As second verification test at intermediate temperature, 35°C was carried out and once again the percentage of the added resistance coming from the polyamide was 85%. At this point there is no clear understanding why these percentages for the added resistance coming from the polyamide for membrane C are equal for different temperatures of the test.
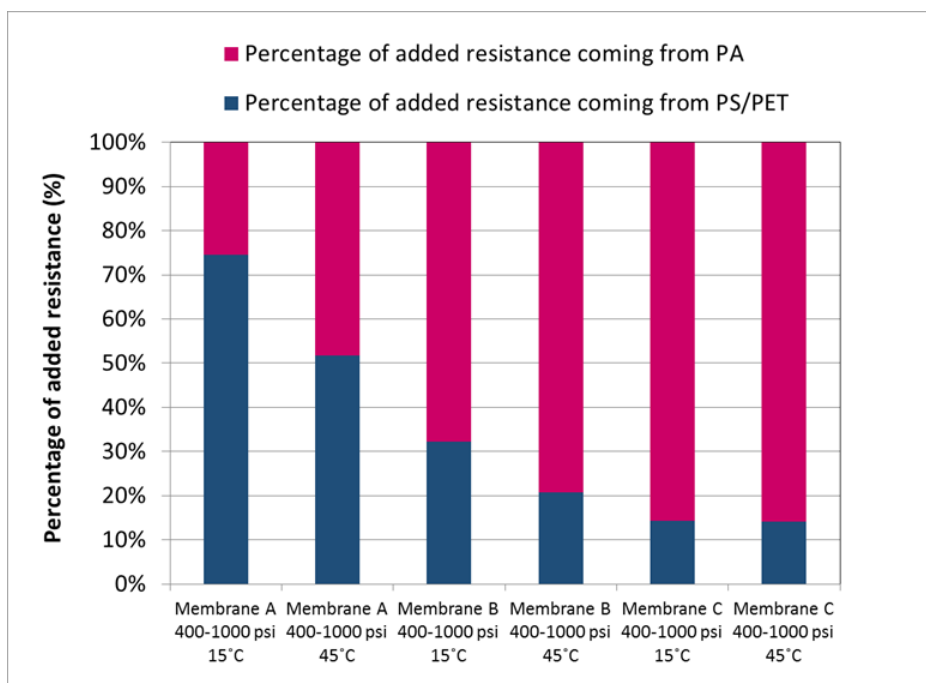
Figure 4.4. Percentage of added resistance of the polyamide and polusulfone/polyester support to the total resistance of the compacted composite

4.4   References

[1].The Dow Chemical Company, FILMTEC Reverse Osmosis Membranes, technical manual, p. 181, Midland, http://www.dow.com/scripts/litorder.asp?filepath=/609-00071.pdf.

5 Chapter 5

Positron annihilation lifetime spectroscopy (PALS) was applied to measure pore size (free volume hole radius) and its distribution in the polyamide layer. The aim was to examine the implication of the microstructure to permeation characteristics of the critical layer. An attempt was made to measure the membrane sample in swollen hydrated state, which is the "real" state of the given membrane during the process of operation. The microscopic swelling might impact on the analysis giving difference in the pore size (ambient vs. hydrated) and may reveal essential information about the membrane state during the process operation. This analysis may allow establishing a structure-performance correlation.

5.1 Analytical Part IV – PALS analyses

Positron Annihilation Lifetime Spectroscopy (PALS) is a unique non-destructive technique for studying nanoscopic open-volume defects, such as vacancies, vacancy clusters, dislocations, nanoprecipitates, nano-porosity, grain boundaries of nano-grains and acceptors (in semiconductors) [1].

In a recent report [2], positron annihilation analysis was applied to detect molecular vacancies or pores of size equivalent to those of salt or hydrated ions in RO membranes. Only a few studies have been done to characterize the free-volume properties of TFC RO membrane using positron annihilation lifetime spectroscopy [3,4,5]. PALS is a unique and valuable technique which characterizes the free-volume hole properties in solid polymeric systems based on the detection of γ-radiation [6,7,8].

Since it is a relatively new technique that expands its application continuously, herein the basic of the technique, the facilities used, data measurements and treatment will be described and lastly the results obtained and its discussion.

5.1.1 Principle of PALS

Positrons are subatomic particles found in the nucleus of an atom. They have the same mass as the electrons, but opposite charge which consider them as their antimatter counter-particles. The positrons have relatively short lifetimes, annihilating in presents of electrons where gamma rays are formed.

Positrons decay in three modes each with its own characteristic lifetime:

(1) The fastest decay mode (free annihilation) occurs when a positron forms a bound state with an electron having an antiparallel quantum spin of the same quantum state. That bound state is similar to the electron cloud formed around a hydrogen atom, and is called "positronium", Ps. A positronium has a diameter of 1.06 Å, the same as the hydrogen atom [9].

(2) Para-Positronium, p-Ps (singlet state $^{1}S_{0}$) formed by electron and positron with antiparallel spins and has a characteristic lifetime of 0.125 ns (Figure 5.1). P-Ps decays by the emission of two 511 keV gamma rays.

(3) Ortho-Positronium, o-Ps (triplet state $^{3}S_{1}$), occurs when the quantum spin states of the two particles are parallel. The o-Ps has a characteristic lifetime in a vacuum of 142 ns, considerably longer than the mean

lifetime of p-Ps. Its decay involves the generation of three 511 keV gamma rays compare with the two produced by the p-Ps decay. The lifetime of o-Ps in matter is also extended relative to p-Ps by the parallel spinning electron, which shields the positron from electrons in the neighboring molecules. This shielding phenomenon causes the o-Ps to become trapped in void sites with diameter between 0.2 pm and 0.5 pm [9].
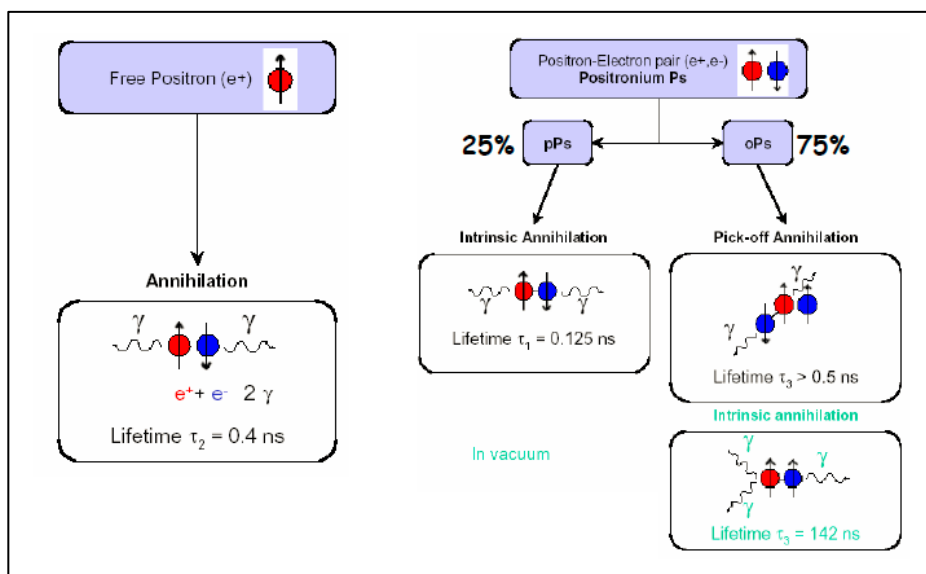
Figure 5.1. Principle of PALS: Ortho-positronium [10]

In condensed media o-Ps does not survive for 142 ns, because the bound electron-positron cloud interacts with other electrons in the matter, shortening the lifetime of the o-Ps. The positrons with initial energy up to 540 keV are rapidly lose their energy by non-elastic interactions when injected into a solid matter, down to thermal energies (~0.27 eV). The thermalization time last just for few picoseconds and the mean positron penetration depth is of the order of 100 μm (Figure 5.2). The travel distance of the positron during the thermallization process depends of the initial positron energy [11].

At the moment of reaching the thermal energies, a positron diffuses in the periodic lattice for 10-100 nm pathway. The positrons have affinity towards the open-volume defects of the structure due to their locally reduced electron density. When trapped in open-volume defects the positron lifetime increases with respect to the defect-free sample. The longer lifetime component which appears in this case gives indication of the size of the open volume. The intensity of this component is directly related to the defect concentration.

Therefore in most of the cases information about the size of vacancy and its concentration can be obtained independently by a single measurement. In fact, that is the major advantage of positron lifetime spectroscopy compared to angular correlation of annihilation radiation or Doppler-broadening spectroscopy with respect to defect/vacancies issues (Figure 5.3) [9,11].

The lifetime of o-Ps in polymers is between 0.5 ns and 3 ns. If there are no voids in the matter being investigated the lifetime of o-Ps will be 0.5 ns [11].
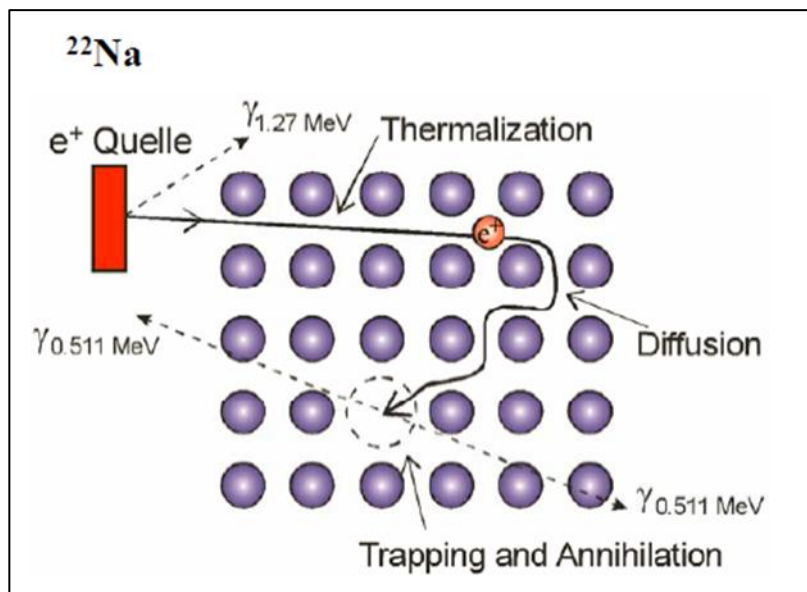
Figure 5.2. Fate of a positron inside matter (thermalization, diffusion through the lattice 10-100nm, trapping and annihilation) [1]
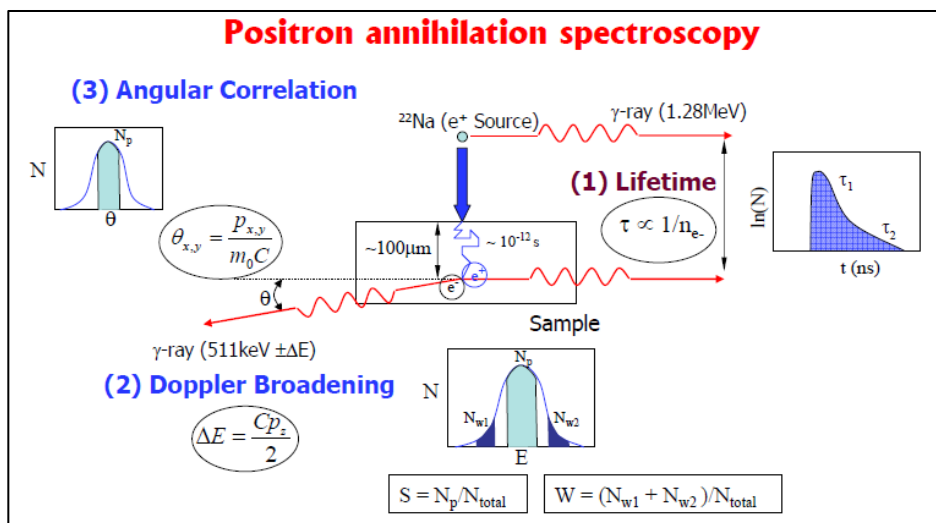
Figure 5.3. Positron Annihilation Spectroscopy consists of three techniques: (1) Positron lifetime (2) Doppler Broadening and (3) Angular Correlation of annihilation radiation [12]

The positron lifetime τ is a function of the electron density at the annihilation site. The annihilation rate λ, which is the reciprocal of the positron lifetime τ, is given by the overlap of the positron density $n_+(\boldsymbol{r}) = |\Psi^+(\boldsymbol{r})|^2$ and the electron density $n_-(\boldsymbol{r})$ [13],

$$\lambda = \frac{1}{\tau} = \pi r_0^2 c \int |\Psi^2(r)|^2 \, n_-(r)\gamma d\boldsymbol{r} \qquad (5.1)$$

r_0 is the classical electron radius, c the speed of light, and $\boldsymbol{r}$ the position vector. The correlation function $\gamma = \gamma[n_-(r)] = 1 + \Delta n_-/n_-$ describes the increase Δn_- in the electron density due to the Coulomb attraction between a positron and an electron. This effect is called enhancement [14].

The o-Ps lifetime, τ_o-Ps, directly correlates with the radius of free volume holes and its intensity (I_o-Ps) contains information about the free volume concentration [15]. The average radius (R) of free volume holes on a quantum mechanical model developed by Tao (1972) and Eldrup et al. (1981) were proposed as follows [16,17]:

$$\tau_{o-Ps} = \frac{1}{2}\left[1 - \frac{R}{R_0} + \frac{1}{2\pi}\sin\left(\frac{2\pi R}{R_0}\right)\right]^{-1} \qquad (5.2)$$

Where τ_{o-Ps} is o-Ps lifetime (ns), R is radius (Å) of free hole space, and R_0 is R +ΔR where the fitted empirical electron layer thickness ΔR is 1.66 Å (Figure 5.4). According to the same model, Figure 5.5 shows the pore radius as a function of the positron lifetime, valid only until 1 nm radius.
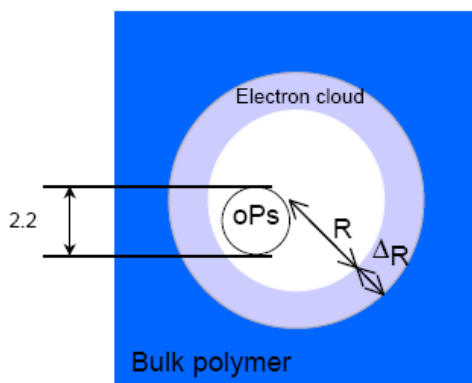
Figure 5.4. Tao-Eldrup model for pore-size estimation ($\leq$ 1nm), approximated as a spherical shape [16]
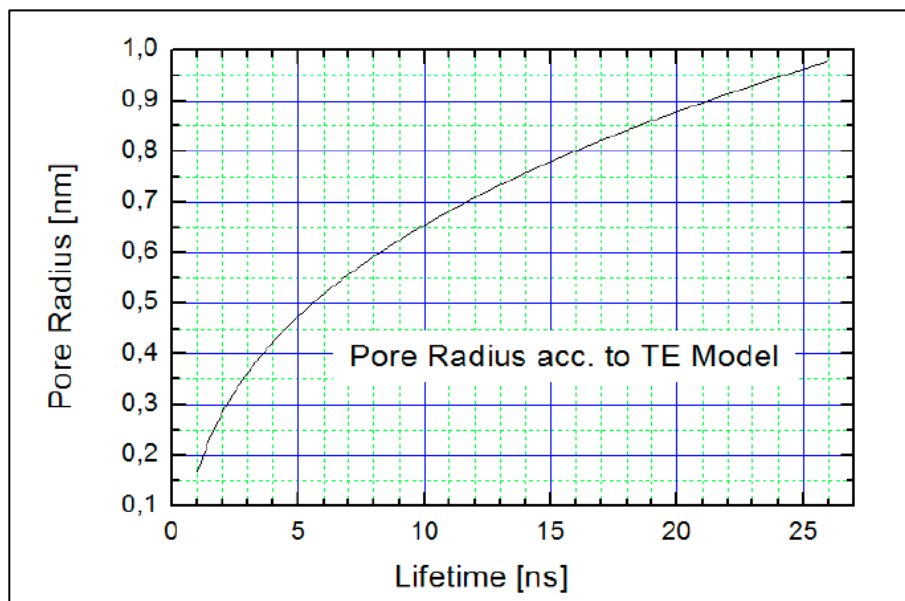
Figure 5.5. Pore radius as a function of the positron lifetime according to Tao-Eldrup model, valid until 1nm radius [16, 17]

5.1.2   Positron generation

Positrons are obtained for laboratory setups usually by the β^+ decay of isotopes. The most popular isotopes are ^{22}Na, ^{64}Cu, ^{58}Co and ^{68}Ge. ^{22}Na has many advantages such as long half-life (2.6 years); short biological half-life; relatively cheap; effective (>90% in β decay) and easy to handle in water solution as ^{22}NaCl or ^{22}Na$_2$CO$_3$. The β^+ decay for ^{22}Na is: ^{22}Na $\rightarrow$ ^{22}Ne + β^+ + v_e + $\gamma_{(1.27MeV)}$ and the decay scheme is given in Figure 5.6. The 1.27 MeV γ appears almost simultaneously with positron - can be used as start event for lifetime. Another way to produce a high flux of positrons (for large scale facilities) is to bombard electrons on an absorber of high atomic number creating Bremsstrahlung γ-rays, thereby generating electron-positron pairs. Positrons can also be produced from nuclear reactors using ^{63}Cu (n,γ) $\rightarrow$ ^{64}Cu or ^{113}Cd (n,γ) $\rightarrow$ ^{114}Cd reaction [1].
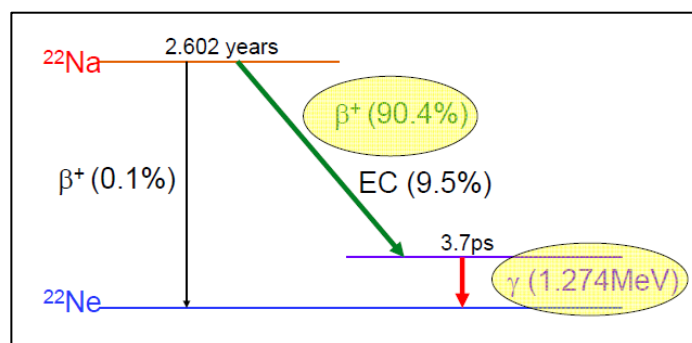
Figure 5.6. Decay scheme of ^{22}Na [12]

5.1.3   Basic of the measurements and data treatment

Experimentally, positron lifetime in a sample is deduced by measuring the time delay between the birth signal (1.28 MeV) and the annihilation signal (511 keV) of a positron using nuclear timing spectroscopy techniques. "*With help of scintillator–photomultiplier detectors the γ-rays are converted into an analog electrical pulses. The pulses are processed by discriminators. Their output pulses start and stop a time-to-amplitude converter as an "electronic stopwatch". The amplitude of the output pulse is proportional to the time difference between the birth and the annihilation γ-quanta and, thus, represents a measurement of the positron lifetime. The single annihilation event is stored after analog–digital conversion in the memory of a multi-channel analyzer. The channel numbers represent the time scale. In order to obtain the complete lifetime spectrum, more than 10^6 annihilation events must be recorded*" [14].

In case of discrete lifetime components the decomposition of the spectra goes by standard computer programs based on Gauss–Newton non-linear fitting routines like: LIFSPECFIT developed by Puska (1978), POSITRONFIT or PATFIT by Kirkegaard et al. (1989) [12,14]. For a continuous distribution of the lifetimes, the data analysis is based on Laplace transformation of the measured spectrum i.e. CONTIN Program by Provencher (1982). Another program that uses linear fitting is also available, MELT program developed by Shuka et al. (1993) [12, 14].

More information about the PALS methods and technique can be found in [12, 18, 19, 20].

Typically positron lifetimes range from a few hundred picoseconds to a few nanoseconds in various materials (metal, semiconductors, insulators, polymers) as given in Figure 5.7.
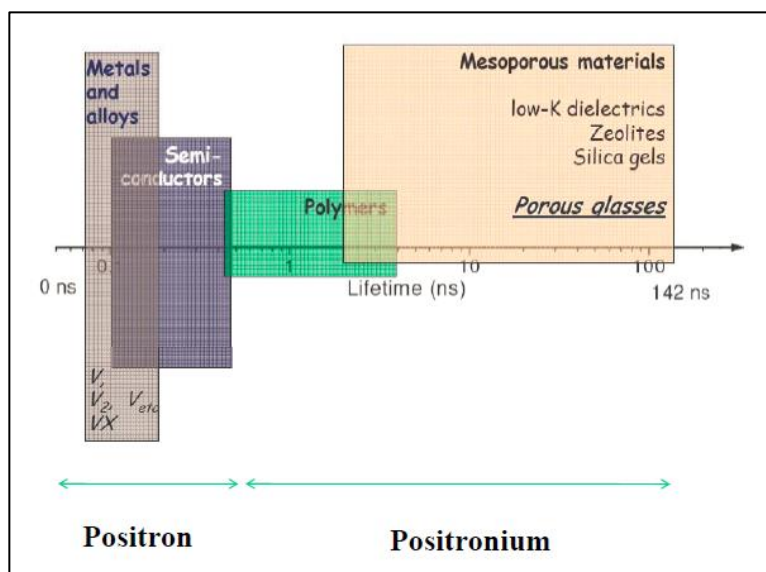
Figure 5.7. Positron lifetimes in various materials [1]

Due to the broad range of depths and depths profiles that can be covered, PALS technique offers certain advantage over the standard techniques used in the material research (Figure 5.8). Each technique has sensitivity over certain size and concentration ranges. In practice combination of few is recommended to unravel complete information.
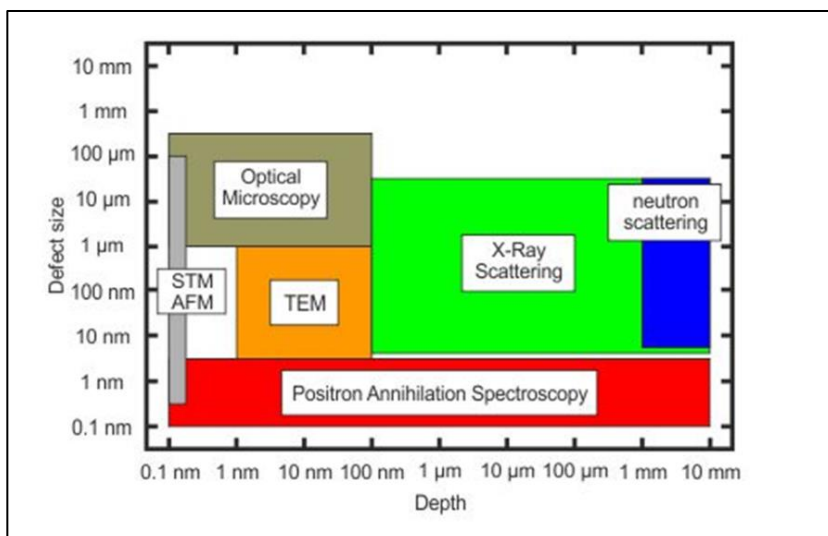
Figure 5.8. Sensitivity of positron-annihilation spectroscopy in comparison to other standard techniques used in materials research [21]

5.1.4   PALS facilities

PALS analyses were performed at ELBE (**E**lectron **L**inac for beams with high **B**rilliance and low **E**mittance) – Center for High-Power Radiation Sources at the Helmholtz Center Dresden-Rossendorf, in Germany [21]. Two complementary setups were used for the purpose. Below is given a short description and the main characteristic for each of them (Table 5.1 and Table 5.2).

Source-Based Positron Spectroscopy - SPONSOR: Source-based positron-sources (like ^{22}Na) are available for complementary and off-beam lifetime measurements (LT) and for depth-dependent Doppler-broadening spectroscopy using a monoenergetic positron beam (Figure 5.9).

Table 5.1. Performance characteristic of SPONSOR

Characteristics of the mono-energetic positron beam SPONSOR	
Accelerating Potential for Positrons	30 - 36 keV
Beam Diameter	d ~ 4 m
Annihilation Energy Resolution	(1.09 + 0.01) keV at 511 keV
Two Germanium Detectors for Coincident Doppler Broadening Spectroscopy	
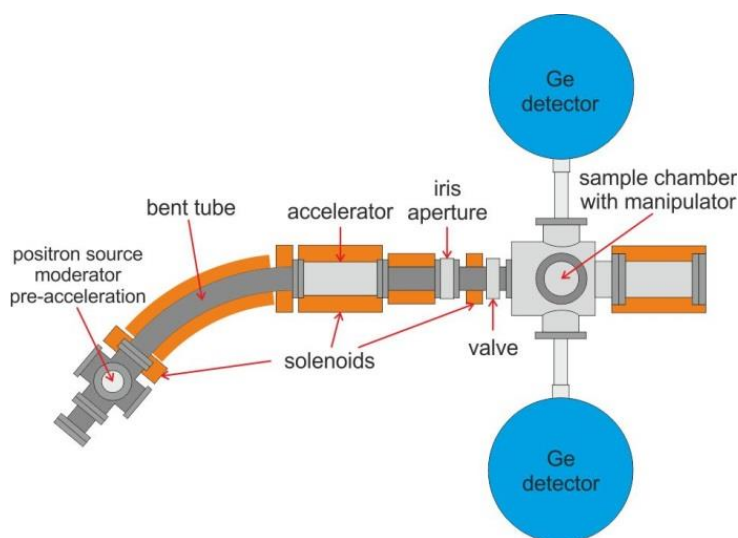
Figure 5.9. Schematics of the monoenergetic positron beam system SPONSOR for depth-resolved defect characterization [21]

Magnetically guided positrons from a [22]Na source of predetermined energies (30 eV – 36 keV) are implanted at depths of up to a few micrometer in the sample. The motion of positron-electron pairs prior to annihilation causes a Doppler broadening of the photopeak in the measured energy spectrum of the annihilation photons characterized by the lineshape parameter S. S is higher for positrons trapped at and annihilated in open-volume defects and it is sensitive to size and concentration of vacancy-like defects. The W parameter ("wing" or core annihilation parameter) is taken at the high-momentum region away from the center. Since the positron annihilation takes place with core electrons, the W parameter probes the chemical surrounding of the annihilation site. The parameters S and W are calculated as the normalized area of the curve in a fixed energy interval (Figure 5.10). The correlation between both parameters varies for different vacancy types [21].
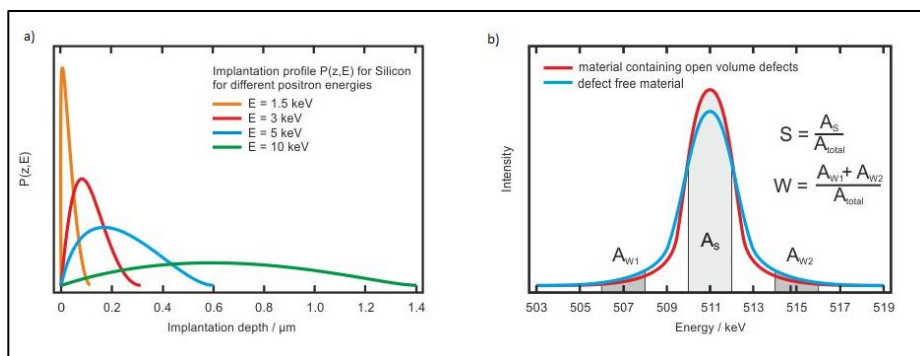
Figure 5.10. Implantation profiles for positron in silicon for various incident energies (a); Definition of line shape parameters S and W for the 511keV two-photon annihilation (b) [21]

The Mono-energetic Positron Spectroscopy – MePS: From the primary ELBE electron beam a monoenergetic positron beam is created by pair production at a tungsten target (Figure 5.11). The unique time structure of the ELBE beam is thereby transferred on the positron beam which results in a pulsed positron source with high repetition rate, high intensity and selectable implantation energies. With this beam measurements at surfaces and thin layers can be performed with high depth resolution.

Table 5.2. Performance characteristics of MePS

Parameters of the positron beam in MePS	
Kinetic Energy	0.5 - 15 keV
Pulse Length	250 ps FWHM[6]
Repetition Rate	1.625 - 13 MHz
Positron Flux	10^6 / s

---

[6] Full width at half maximum
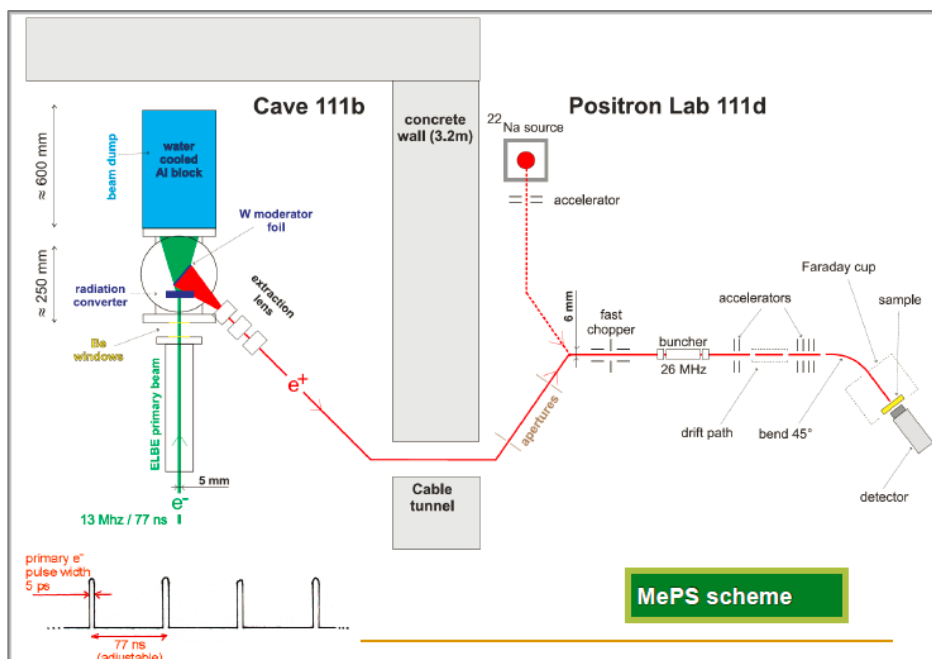
Figure 5.11. Schematics of the monoenergetic positron beam system MePS [21]

5.2 Methodology

Several aspects were set up in the focus of these analyses. But the main intention and final objective for applying this technique was to study if any change in the pore size of the polyamide voids is present in compacted polyamide membranes compared with membrane that have never been operated. Finally this objective was not fully accomplished. The application of PALS for studying the polyamide materials is in a very early stage, thus there are concerns about the method used (and published earlier in the literature), the results treatment and interpretation. There is lack of standardize methodology and correlations that will describe the implication of the microstructure to permeation characteristics of the critical layer. Not all measurements conducted regarding this research were successful due to variety of reasons, nevertheless a series of supplementary testing is needed to optimize the method and get to the point of extracting valuable results.

This chapter covers the analysis of the pore size (free-volume hole radius) and its distribution in the polyamide layer when the membrane is "dry" i.e. on room conditions and analysis of the polyamide pores when the sample is exposed to certain level of humidity.

The climate test chamber (model Vötsch Industrietechnik) had the following specifications: chamber volume of 190 Liter, maximum temperature range -72˚C up to +180˚C, for climate simulations +10 ˚C to +95˚C, humidity range 10% up to 98%, dew point -3˚C up to +94˚C.

PALS can offer a unique opportunity to measure membrane samples in a swollen hydrated state, which is the "real" state of the given membrane during the process of operation. The basic definition for the swelling phenomenon was given earlier in section 3.1.2 of the third chapter. Once more, swelling is the process of dissolution of a polymer in a defined solvent [22], while the microscopic swelling observation is defined as the increase in the equivalent Bragg spacing as a result of solvation, inferred from small-angle X-ray scattering (SAXS) data [23, 24]. This analysis may allow establishing structure-performance correlation.

The main linear accelerator (LINAC) beam parameters were: continuous waveform (CW); E = 30 MeV, I = 40-90 µA, 26 MHz. The MePS set up conditions were:

1. For the reference samples set: E=1 keV and 3.6 keV at 5Mio and E=6 keV and 12 keV at 25Mio total counts for sufficient statistic in order to perform pore size distribution analysis in the PA layer

2. For the humidity test: E=1 keV and/or 3.6 keV at 30Mio counts

The short life time component was 50 ns considering 3.1912 ps/channel and the long lifetime component was 1000 ns with 60.4435 ps/channel.

5.2.1   Samples preparation

Samples selection for this analysis included membrane D, C and A membrane flat sheets. This series offers board range of performance characteristics in terms of permeability, salt rejection and boron rejection (Table 5.3). Those values are given in the product data sheet of the elements [25] meanwhile the boron rejection of membrane D was found in the literature [26]. Testing conditions were: temperature 20˚C, permeate flux 40L/m^{2}h, cross flow velocity 30.4 cm/s, 4.6 mg/L as boron in the feed. The motivation of introducing an NF membrane was to confirm on the reliability of the PALS measurements.

Table 5.3. Membrane product specification for D, C and A rolled as spiral wound elements at given active area

Membrane type	Permeability	Salt rejection	Boron rejection
D [400 ft^2]	10,000 gpd	97.00%	18%
C [440 ft^2]	17,000 gpd	99.70%	89%
A [400 ft^2]	6,000 gpd	99.82%	93%

Membrane samples of 2 cm x 2 cm were cut from corresponding rolls of D, C and A. There was no other pre-preparation protocol like wetting, cleaning or similar. The samples labeled as PAM 1B, PAM 2-3 and PAM 3B were first measured dry and then subsequently exposed to 70% and 90% of humidity at 25˚C during 2h in the climate chamber and again measured at MePS (Table 5.4). Additional sample, PAM 2-4 was taken as dry control sample and repetitive measurements were performed on it.

Table 5.4. The five steps taken to conduct the humidity test

Sample	1	2	3	4
Label	PAM 1B	PAM 2-3	PAM 3B	PAM 2-4
Membrane type	D	C	A	C
Step 1 (MePS)	Measure at MePS	Measure at MePS	Measure at MePS	Measure at MePS
Step 2 (Climate chamber)	70%, 25˚C, 2h	70%, 25˚C, 2h	70%, 25˚C, 2h	Out of the chamber (room conditions)
Step 3 (MePS)	Measure at MePS	Measure at MePS	Measure at MePS	Measure at MePS
Step 4 (Climate chamber)	90%, 25˚C, 2h	90%, 25˚C, 2h	90%, 25˚C, 2h	Out of the chamber (room conditions)
Step 5 (MePS)	Measure at MePS	Measure at MePS	Measure at MePS	Measure at MePS

5.3   Results and discussion

5.3.1   Preliminary Doppler Broadening results

Preliminary analyses were performed at SPONSOR setup in order to estimate defects (pore) distribution across the sample thickness. The intention was to estimate the region of interest with respect to positron energy that is essential for the lifetime measurements execution. Moreover, a lot of useful information can be already acquired, like ortho-Positronium (o-Ps) distribution in the layer (it is basically an evidence of voids/pores), indirectly defect type and its concentration if there are.

Depth sensitive Doppler broadening (DB) and classical sandwich type lifetime (cLT) measurements were performed on three reference samples PAM1 (D), PAM2 (C) and PAM3 (A). From DB measurements the annihilation line parameter S (Figure 5.12 a) and 3/2 gamma ratio values were extracted (Figure 5.12 b). The S-parameter clearly shows differences in defect concentration between samples across the PA layer thickness, whereas 3/2 gamma ratio indicates increased o-Ps formation at PA and its interface with the polysulfone layer. The 3 gamma annihilation has been acquired from a linear region before

the annihilation peak, whereas the 2 gamma annihilation represents the number of counts from ±70 channels around the 511 keV annihilation line. The cLT measurement was performed in order to investigate porosity of the 40 µm polysulfone layer. Two identical membranes have been sandwiched with ^{22}Na source and two Si substrates. The membranes are very thin thus most of the signal comes from silicon (about 72%). Nevertheless, two longer positron lifetime components were detected: 1.92 ns and 77.6 ns with corresponding intensities of 7.7% and 0.23%, respectively. They are a fingerprint of the pore size of 0.28 nm (radius) and 2.48 nm, respectively according to the modified extended Tao Eldrup model. As an example, the classical lifetime spectrum of sample PAM3 is given (Figure 5.13) showing very good fit between the experimental data and the software. In order to resolve the pore size and its distribution variable positron energy lifetime measurements are necessary.

In a similar way, additional samples collected after operation (Figure 5. 14) were analyzed. The results are indicating a change in the defect concentration between the reference and compacted samples in a way that there are less and bigger pores. In fact, it can be noticed that the seawater membranes after operation (PAM4 to PAM7) have similar profile for defect concentration as the nanofiltration reference (membrane D). However the quantitative information of the pore size and distribution could be extracted only from the lifetime measurements using variable positron energy.

Initial measurements were performed applying the same principle, with a purpose of evaluating if any changes in the pore size under different climate simulations i.e. ambient vs. swollen hydrated state of the membrane. For this occasion, first two samples from PAM2 (C), one dry and other that was exposed for 2 hours in climate chamber at 25°C and 90% humidity (red trends on Figure 5.15) were taken. At first glance there is clear difference between the reference-dry membrane and hydrated one. In order to verify that the effect was reproducible another pair of membranes was taken to repeat the analysis (results given in black trend Figure 5.15). It was noticed that the both reference samples are also showing differences between each other which leads us to high variability due to the local inhomogeneous characteristics of the polyamide layer. To overcome this problem in the subsequent lifetime analysis, it was decided to use the same sample cut and perform all the consecutive analysis on it as per Table 5.4.

It is worth mentioning that there was no method in place to measure the amount of water that was absorbed by the membrane. The challenge

encountered here was to hydrate the membrane without having water drops in it. The only check done here was to monitor the S-parameter using the Doppler broadening method during the first 30 minutes of the measurements to ensure that there is no outgassing present that might influence the results. Additional variety in the results might come from the different absorbing capacity of membrane that has been prepared differently.
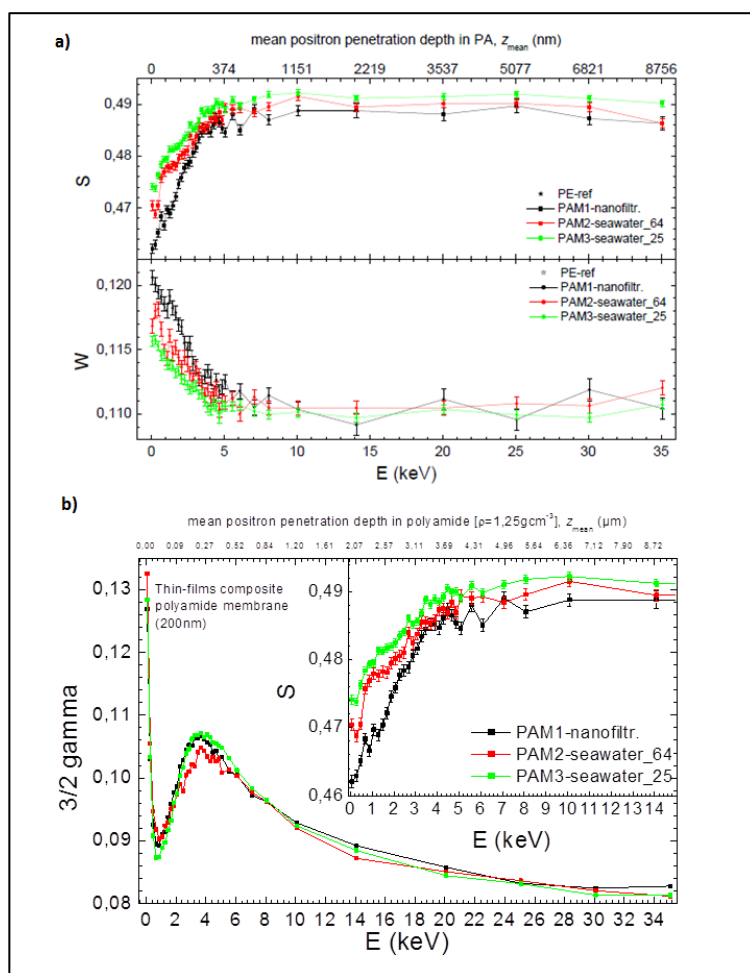
Figure 5.12. Defect concentration (S-parameter) (a) and 3/2 gamma ratio (b) as a function of positron energy, E and mean positron penetration depth, z_{mean}
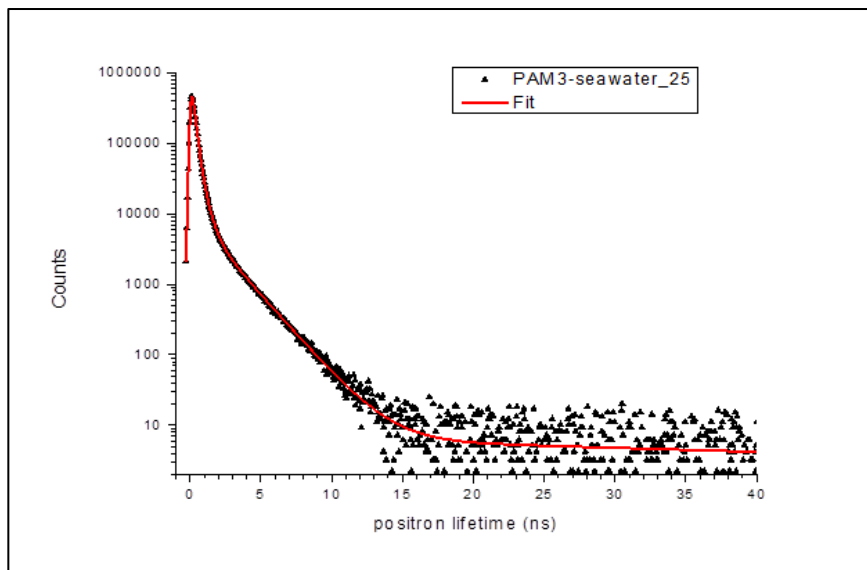
Figure 5.13. Classical life time spectrum with corresponding fit (PALSfit software [12])
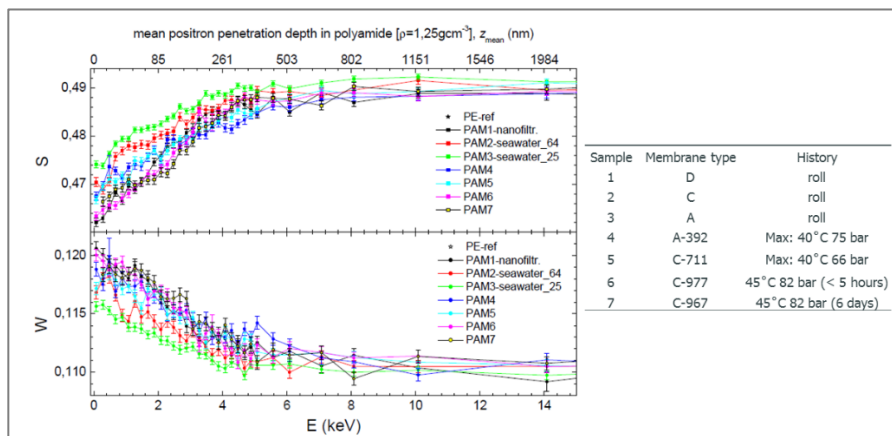
Figure 5. 14. S (E) dependencies of the reference and compacted samples
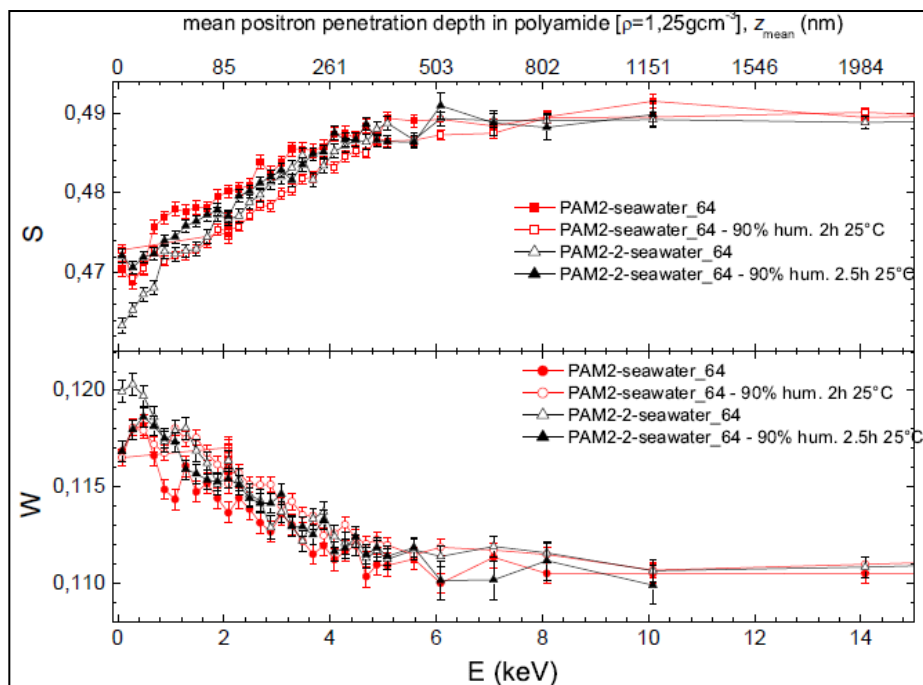
Figure 5.15. Defect concentration, S as function of positron energy, E for dry and hydrated state of the membrane

5.3.2 Ambient vs. hydrated state of the membrane studied with PALS

As given earlier the aim of this analysis was to study the effect of dry and swollen hydrated state of the membrane in respect to the open pores in the polyamide structure. Moreover this section discusses the results obtained of probing different depths of the film composite membrane.

In total four different lifetime components were identified for all three membranes with applying variable positron energy (1, 3.6, 6 and 12 keV). The mean positron penetration depth with the given energies will be between 29-1613 nm. However in most of the cases only two to three lifetime components were meaningful i.e. could be correlated with specific pore radius, and the sum of their intensity was always below 25%. The other two lifetime components which gave relatively high intensity > 75% had lifetime values lower than 0.6 ns. This means that from all decay events monitored only less than 20% gave information for the pores size while the rest belongs to passing positron, self-annihilated positrons, p-Ps or positrons that were not trapped within the membrane film structure. Another cut-off is that the lifetimes with intensity lower that 1% in practice is considered as not significant. Nevertheless they will

103

be given here because they reflect bigger pores sizes that are present in the structure (sometimes in literature referred as aggregate pores). Although minority in concentration they will play certain roll in the transport mechanism, especially on the salt rejection thus they are included in the comparison of the different membrane types.

Figure 5.16 gives the summary of the lifetime and intensity of the all four component observed for membrane D, C and A as a function of the positron energy. Taking closer look to plots a), c) and e) it can be noticed that the highest lifetime is given by the forth component and with that we have the pores with bigger radius. Other important info from these plots is that those pores are getting smaller when increasing the probing depth. Those finding are expected knowing that those pores with radius of ~1.5 nm can be found in the polyamide and the interlayer between the polyamide and polysulfone, but not or very rarely in the bulk of the polysulfone (where the pores can be hundreds of nanometers and often macro voids can be found as well). The positrons would not be trapped in those big pores and thus not further information can be extracted with this technique.
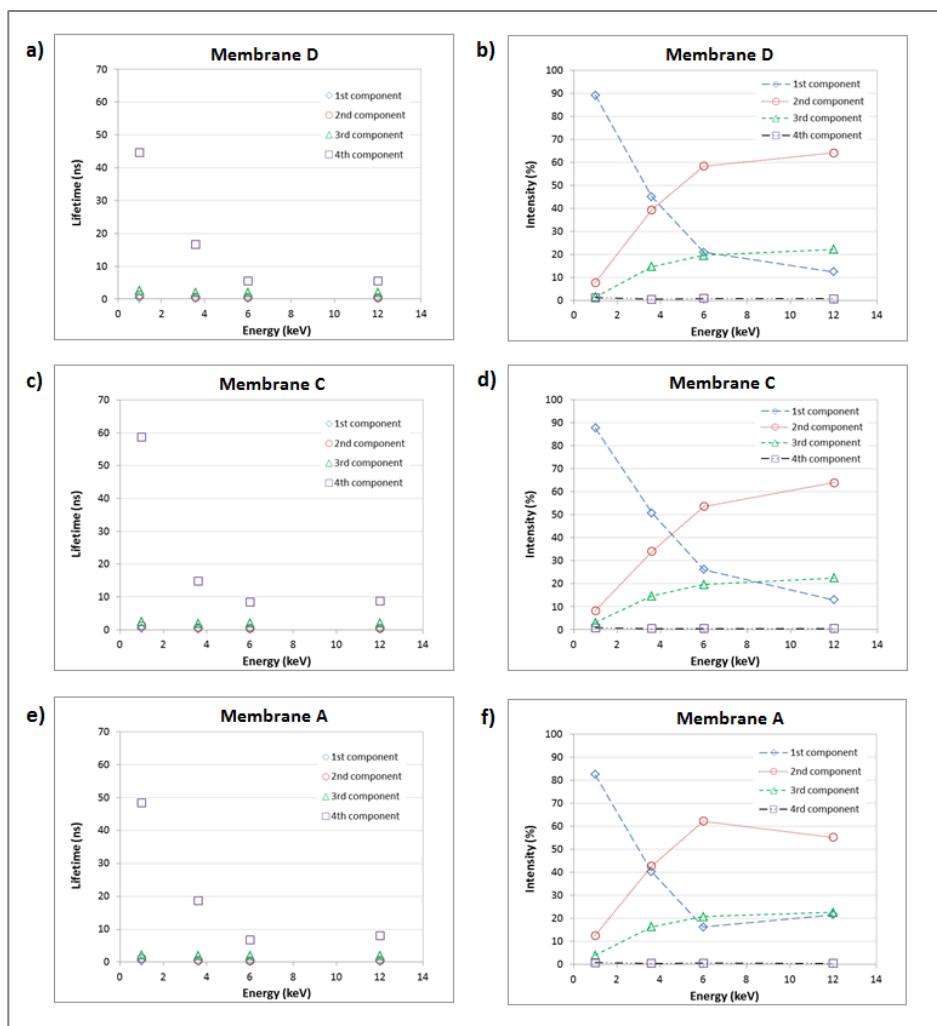
Figure 5.16. Lifetime (a,c,e) and intensity (b,d,f) of the all four component observed for membrane D, C and A as a function of the positron energy

On the other hand the intensity of those pores is very low as seen on Figure 5.16 b), d) and f). Those plots show that the intensity i.e. distribution of the lifetime components is changing depending on the probing depth.

Two energies were selected to probe the pore size on dry and hydrated membrane state, 1 keV and 3.6 keV. The most relevant results extracted are given in Table 5.5 which summarizes the values of the o-Ps lifetime, their intensity and the corresponding void radius at energy of 1 keV for the three membrane types. The main conclusions are:

Two type of pores were identified in range 0.20 – 0.33 nm and 1.4 – 6.69 nm on room condition state of the membrane. It is interesting to see that the pores with radius 0.20 – 0.33 nm were present in all membrane, but with significant difference in intensity i.e. concentration. The correlation made here is that the better rejecting membrane has higher concentration from those sizes of pores. For instance, pores with radius of ~0.20 nm show intensity of 7.8%, 8.4% and 12.6% for D, C and A respectively. The bigger pore radius from 1.4 nm was found in D, 6.6 nm in C and 1.5 nm in membrane A. The intensity of those pores is lower in the case of A, almost to the border of being statistically insignificant. In the case of C the intensity of the 6.6 nm pores is 2% which makes them statically significant portions of the total numbers of pores in the polyamide layer. Moreover the 6.6 nm is relatively high pore radius. Maybe the bigger pore radius observed here (1.4 – 6.69 nm) has some role with the membrane permeability, as C is the highest permeability membrane of the series. It was reported earlier in the literature [3], that there are two types of pores in the membrane surface, i.e. network pores and aggregate pores as illustrated on Figure 5.17. The network pores are the small spaces between polymer segments constituting the polymer aggregate, whereas the aggregate pores indicate the large spaces surrounding the polymer aggregates.
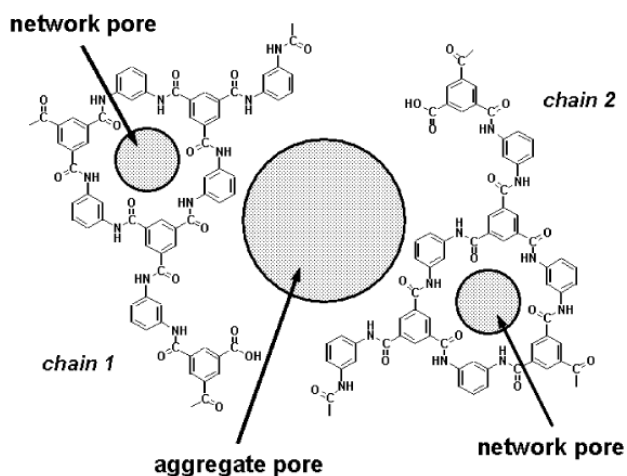
Figure 5.17. Schematic representation of possible molecular structure of network and aggregate pores in aromatic polyamide TFC membranes [3]

The measurements were repeated after exposing the membrane samples in climate chamber for two hours at 25°C and 90% of humidity. The hydrated pore radius is smaller than the radius measured on dry membrane in such a way that there is 15% average reduction on the smaller pores radii and up to 38% average reduction of the bigger pores radii. Looking individually per membrane type the highest percentage of reduction was noted for the highest performing rejection membrane A. This information can have huge impact on the current understanding about the performance of the critical layer. From one side all PALS measurements previously reported are on dry membranes which may not reflect fully the membrane state during real operation. On the other side the reduction seen here will play critical role in the rejection of the monovalent, divalent ions and neutral species. With respect to the question why we are observing smaller pore radius of hydrated membrane one possible explanation could lay in the change of the hydrogen bond length. One case is that end groups are bonded with hydrogen atom or if there is force attraction of neighboring -NH and –CO groups in building weak to strong hydrogen bonding. The hydrogen bond by its length can vary between 1.5 – 2.5 Å [27]. The donor-acceptor distance can also vary depending of the bond type: strong, mostly covalent bond from 2.2 – 2.5 Å; moderate, mostly electrostatic 2.5 – 3.2 Å or weak, electrostatic by nature 3.2 – 4.0 Å [27]. With expending of the certain section of the PA structure in the network the free volume in between will get more occupied with molecules, which results in reducing its radius. Nonetheless further investigations are needed to give firm conclusions.

Table 5.5. Summary of the o-Ps lifetime, their intensity and the corresponding void radius at energy of 1 keV

E=1 keV Depth 29 nm	Ambient conditions			After 2h at 25°C and 90% humidity		
	o-Ps (ns)	I (%)	Free volume hole radius (nm)	o-Ps (ns)	I (%)	Free volume hole radius (nm)
Membrane D	1.24	7.86	0.20	1.13	5.18	0.19
	2.57	1.69	0.33	2.26	1.59	0.31
	44.60	1.24	1.46	20.10	0.41	0.96
Membrane C	1.36	8.41	0.22	1.19	8.09	0.20
	2.62	2.61	0.34	2.35	1.86	0.32
	105.33	2.07	6.69	96.56	2.31	4.30
Membrane A	1.24	12.63	0.20	0.67	18.64	0.10
	2.16	4.03	0.30	1.72	10.3	0.26
	48.33	0.86	1.55	16.34	0.34	0.85

The probing at 3.6 keV (Table 5.6) did not reveal changes in the free volume pore radius after two hours exposure to 25°C and 70% humidity and 25°C and 90% humidity, respectively. Only one meaningful component was identified with corresponding pore size of ~0.29 nm. The second lifetime component with corresponding pore size of ~0.84 nm has intensity level lower than 1%. With these conditions we are most probably probing the interlayer between the polyamide and polysulfone, thus further testing might be needed with longer exposure time in the climate chamber.

Table 5.6. Summary of the o-Ps lifetime, their intensity and the corresponding void radius at energy of 3.6 keV

E=1 keV Depth 29 nm	3.6 keV ambient conditions			3.6 keV (2h, 25°C, 70%)			3.6 keV (2h, 25°C, 90%)		
	o-Ps (ns)	I (%)	Free volume hole radius (nm)	o-Ps (ns)	I (%)	Free volume hole radius (nm)	o-Ps (ns)	I (%)	Free volume hole radius (nm)
Membrane D	2.03	14.83	0.29	2.03	14.98	0.29	2.04	14.98	0.29
	16.58	0.63	0.85	20.50	0.72	0.97	18.90	0.63	0.94
Membrane C	1.94	14.63	0.28	1.96	14.25	0.28	1.96	14.28	0.28
	14.77	0.47	0.81	18.56	0.50	0.90	16.15	0.48	0.84
Membrane A	1.95	16.34	0.28	1.97	16.49	0.28	1.98	16.31	0.28
	18.74	0.54	0.93	13.41	0.46	0.77	25.32	0.72	1.07
Membrane C (control dry)	1.97	14.75	0.28	1.97	14.67	0.28	1.99	14.49	0.28
	15.96	0.50	0.84	15.78	0.50	0.84	17.33	0.51	0.87

5.3.3 Recommendation

Based on the experience applying PALS technique for measuring free volume pore size in TFC membranes and the challenges found, here are given few recommendations:

- To probe the polyamide layer the correct energies are 1-3 keV;
- There is not clear understanding at the moment how the coating (present in some commercial membrane) may affect the results. This will be important when comparing coated and uncoated membrane at the same probing depth;
- Systematic study is needed to understand the effect of different variables on the change of the free volume pore size, for instance: temperature 25-45°C, humidity level 70-95%, time of exposure 2-12h and depth profiling 30-180 nm;
- Once the method is validated, dry and with humidity, compacted samples can be measured.

5.4 References

[1]. Krause-Reinhard, R. Fundamentals of positron annihilation lifetime spectroscopy and it application in semiconductors. Martin-Luter University Halle-Wittenberg, Germany

[2]. Shimazu, A., Ikeda K., Miyazaki T., Ito Y. (2000) Application of positron annihilation thechnique to reverse osmosis membrane meaterials. *Radiation Physics and Chamistry* 58, 555-561.

[3]. *Kim, S. H., Kwak, S-.Y., Suzuki, T. (2005) Positron annihilation spectroscopic evidence to demonstrate the flux-enhancement mechanism in morphology-controlled thin-film composite (TFC) membrane. Environmental Science & Technology 39, 1764-1770.*

[4]. Fujioka, T., Oshima N., Suzuki R., Price W.E., Nghiem L.D. (2015) Probing the internal structure of reverse osmosis membranes by positron annihilation spectroscopy:gaining more insight into the transport of water and small solutes. *Journal of Membrane Science* 486, 106-118.

[5]. Fujioka, T., Oshima N., Suzuki R., Khan S.J., Roux A., Poussade Y., Drewes, J.E, Nghiem L.D. (2013) Rejection od small and uncharged chemicals of emerging concern by reverse osmosis membranes: The role of free volume space within the active skin layer. *Separation and Purification Technology* 116, 426-432.

[6]. Jean, Y.C., Mellon, P.E. and Scharader, D.M. (2003) Principles and Applications of Positron and Positronium Chemistry . World Scientific, Singapore

[7]. Shantarovich, V.P., Suzuki, T., He, C., Davankov, V.A., Pastukhov, A.V., Tsyurupa, M.P. et al. (2002) Positron annihilation study of hyper-cross-linked polystirene networks. *Macromolecules* 35, (26), 9723–9729.

[8]. He, C., Suzuki, T., Ma, L., Matsuo M., Shantarovich V.P., Kondo K., Ito Y., (2002) Molecular motions at low temperature observed by positron annihilation. *Physics Letters* 304, 49-53.

[9]. Bigg, D.M. (1996) A review of positron annihilation lifetime spectroscopy as applied to the physical aging of polymers. *Polymer Engineering and Science* 36, (6), 737-743.

[10]. Krause-Reinhard, R. Positron annihilation as a tool in materials science. Martin-Luter University Halle-Wittenberg, Germany

[11]. Kobayashi, Y., Haraya, K. and Hattori, S. (1994) Evaluation of polymer free volume by positron annihilation and gas diffusivity measurements. *Polymer* 35, 925-928.

[12]. Positron lifetime spectroscopy, tutorial. Available from: http://www.positronannihilation.net/index_files/Page434.htm, accessed 10.10.2106

[13]. Nieminen, R.M., Manninen, M.J. (1979) Positrons in imperfect solids: theory. P. Hautojarvi, ed., (p. 145.),Springer, Berlin

[14]. Krause-Rehberg, R.,Lepiner, H.S.(1998) Positron annihilation in semiconductors. Springer, Verlag, Berlin

[15]. Wang, Y.Y., Nakanishi, Y., Jean, Y.C., Sandrecki, T.C. (1990) Positron annihilation in amine-cured epoxy polymers-pressure dependence. *Journal of Polymer Science* 28, (9), 1431-1441.

[16]. Tao, S.J. (1972) Positron annihilation in molecular substances. *Journal of Chemical Physics* 56, 5499.

[17]. Eldrup, M., Lightbody, D., Sherwood, J.N. (1981) The temperature dependence of positron lifetimes in solid pivalic acid. *Chemical Physics* 63, 51-58.

[18]. Coleman, P. (2000) Positron beams and their applications. World Scientific Publishing, Signapore.

[19]. Charlton, M., Humbertson, J.W., (2001) Positron Physics. Cambridge University Press, UK.

[20]. Lopez-Castanares, R., Olea-Cardoso, O., Vazquez-Moreno, F., Lizama-Soberanis, B., Camps-Carvajal, E., Angeles-Anguiano, E., Castano, V. (2002) Positron annihilation for characterizing polymeric materials. Bulgarian Journal of Physics 29, 155-178.

[21]. Helmholtz-Zentrum Dresden-Rossendorf, Germany. Oficcial web page: http://www.hzdr.de/db/CMS?pNid=363, accesssed October 2016.

[22]. Izak, P. (2007) Swelling of the polymeric membranes in room temperature ionic liquids. *Journal Membrane Science* 296, 131-138.

[23]. Gebel G. (2000) Structural evolution of water swollen perfluorosulfonated ionomers from dry membrane to solution. *Polymer* 41, 5829-5838.

[24]. Fujimura, M., Hashimoto, T. and Kawai, H. Small-angle X-ray scattering study of perfluorosulfonated ionomer membranes 2. Models (1982) for ionic scattering maximum. *Macromolecules* 15, 136-144.

[25]. The Dow Chemical Company, Midland, 2016. Available from: http://www.dow.com/en-us/water-and-process-solutions/products

[26]. Tu, K. Le., Nghiem, L. D., Chivas, A. (2011). Coupling effects of feed solution pH and ionic strength on the rejection of boron by NF/RO membranes. *Chemical Engineering Journal*, 168 (2), 700-706.

[27]. Jeffrey, G. A., (1997) An introduction to hydrogen bonding. Oxford University Press, UK.

6 Chapter 6

This is the final chapter of the thesis and thus provides results interpretation and an overview from previous chapters. Furthermore it expends the results discussion towards conclusions by linking back to the objectives and the hypothesis set up on the beginning. In addition this chapter offers ideas that can be used for future research in a more systematic manner. The authentic about this work is that it shows new approaches and defines new areas towards fundamental understanding of the performance of reverse osmosis membranes. Generating knowledge at this scale can empower an open more space for future innovation.

6.1 Summary and outlook

6.1.1 Chapter 1

The first chapter provides the big picture, looking into the water scarcity as one of the main concern of today, than the reverse osmosis technology as possible and attractive solution, the research interest by the academic community for developing in this area and finally the market forecast suggesting that water will become $30 billion industry by 2025.

The scope of this study is a phenomenon known as compaction. Membrane compaction refers to the physical compression of the RO membrane itself. This compression results in a decrease in flux (and often an increase in the salt rejection). The rate of compaction is directly proportional to an increase in temperature and pressure. The objective of this study is to gain fundamental understanding for the compaction phenomena and its implication to the transport mechanism.

The main research hypothesis is that there is an irreversible portion of the flow reduction due to structural changes in the PA chemistry. The statement by itself is opposite to common belief, as the PA is considered to have a very stable structure that is not affected within the typical operating range (temperature up to 45°C and pressure up to 82 bar).

6.1.2 Chapter 2

The second chapter was focused on describing the physical changes observed in the RO TFC membrane layers regarding to its surface morphology and thickness.

The AFM analysis showed no linear relationship between membrane surface roughness and its permeability rate for three different SWRO membrane types: A, B and C. It was also observed that the membrane surface roughness showed decreasing trend after operation: 10-20% decrease in the surface roughness of the samples tested on a flat cell bench (at condition of 15 bar and 25°C) and almost 40% decrease for the compacted samples from elements (that were operated on 45°C and 82 bar).

A potential diagram is proposed (Figure 6.1) that builds the correlation between different parameters characterizing the polyamide structure. It shows that the surface roughness could be correlated only with the cross-linking rate of the polyamide, and then the cross-linking rate can be used to judge the permeability rate. No relationship could be drawn going directly from the

113

surface roughness to membrane permeability rate as there is no eligible parameters that can be measured that intrinsically connect them. However series of testing are needed controlling all three parameters to confirm on this relationship triangle.

The SEM analysis revealed polysulfone material passage through the polyester web fibers. ESEM cross-section images showed that the total membrane thicknesses is reduced by 33.5 μm (23% of the initial thicknesses of the roll sample) from which 21.5 μm or 14.8% belongs to the polyester web layer and 11.9 μm or 8.2% to the polyamide and polysulfone layer. The statistical analysis showed that those changes are significant. A lower thickness of the PS layer is consequence of a denser structure and collapsed pores. Those collapsed pores were initially giving free passage to the water flow, but afterward they block the water pathway. Further experiments and computational model analysis are needed in order to quantify the rate of water restricted per units of area.
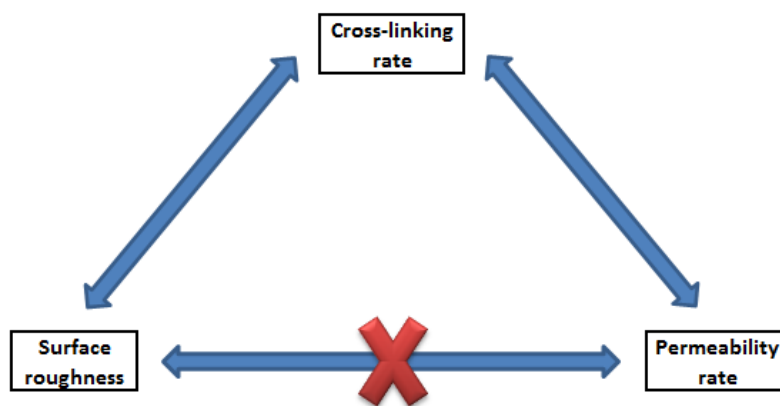
Figure 6.1. Relationship triangle between surface roughness, cross-linking rate and permeability rate of a membrane in describing its characteristics

6.1.3   Chapter 3

The third chapter combines several analytical techniques to evaluate any changes in the chemical content of the polyamide structure in compacted RO samples. Here are the main conclusions per analysis:

XPS analysis reveal changes in the carbon bonding structure of the compacted membrane samples compared to their reference in a way that the C-C bonding rate shows a decreasing trend, the C-O or C-N show an increasing bonding

range and the same for C=O or O=C-N. The changes identified were comparable between the three chemistries studied A, B and C.

The O/N ratio in the membrane samples after operation is more than 65% higher than in the reference samples. This may indicate changes in the cross-linking rate of the polyamide, from being fully cross-linked before the operation to having mostly linear structure after the process operation.

Portion of all analysis conducted in this part use proprietary, unpublished experimental methods and for the sake of confidentiality have been omitted from this version of the thesis.

6.1.4   Chapter 4

The chapter four aims to segregate compaction flow loss between its constituents (polyamide and polysulfone) and determine if any sizeable portion of the total flow loss (under certain temperatures and pressure) is due to the polyamide compaction. The results are indeed suggesting that significant percentage of added resistance is coming from the polyamide layer, 25% to 85% depending of the membrane chemistry at conditions of 15°C and pressure increase from 28 bar to 69 bar. Moreover at elevated temperature (45°C) those percentages tend to increase, meaning the contributions of compacted polyamide layer is becoming greater than 50% and thus cannot be neglected.

6.1.5   Chapter 5

Positron annihilation lifetime spectroscopy (PALS) was applied to measure the pore size (free volume hole radius) and its distribution in the polyamide layer in ambient and hydrated state. Two type of pores were identified in range 0.20 – 0.33 nm and 1.4 – 6.69 nm on room condition state of the membrane. It is interesting to see that the pores with radius 0.20 – 0.33 nm were present in all membrane, but with significant difference in intensity i.e. concentration. The correlation made here is that the better rejecting membrane has higher concentration from those sizes of pores. The bigger pore radius was 1.4 nm in D, 6.6 nm in membrane C and 1.5 nm in A. The intensity of those pores is lower in the case of A, almost to the border of being statistically insignificant. In the case of membrane C the intensity of the 6.6 nm pores is 2% which makes them statically significant portions of the total numbers of pores in the polyamide layer. Maybe the bigger pore radius observed here (1.4 – 6.69 nm) has some role with the membrane permeability, as C is the highest permeability membrane of the series. The hydrated pore radius is smaller than the radius measured on dry membrane in such a way that there is 15% average reduction

on the smaller pores radii and up to 38% average reduction of the bigger pores radii. This information can have huge impact on the current understanding about the performance of the critical layer. From one side, all PALS measurements previously reported are obtained on dry membranes which may not reflect fully the membrane state during real operation. On the other side, the reduction seen here will play a critical role in the rejection of the monovalent, divalent ions and neutral species. PALS technique can be very beneficial in discovering more about the polyamide characteristic on fundamental level.

6.2 Thesis conclusions

The work done in this thesis was dedicated to get insight in the changes that the membrane experiences after the process operation and gain better understanding on the compaction phenomenon. Based on all results gathered, herein is given simplistic description and broad definition of the compaction phenomenon:

When operated at elevated conditions of temperature and pressure (45°C and 82 bar), SWRO membranes might suffer compaction, as a result of physical changes in the polysulfone layer and chemical content changes of the polyamide layer. Those changes affect the membrane performance irreversibly. Moreover the predicted membrane performance after compaction will be a complex combination of consequences. For instance, as XPS results suggested the polyamide cross-linking rate is changing from fully cross-linked to mainly linear, therefore we should expect that the permeability of the membrane will increase and the salt passage will increase as well, if that is the only change seen in the entire composite membrane (Table 6.1). But in non-ideal case we also have physical changes of the polysulfone. As we have seen with ESEM analyses the polysulfone layer is getting denser and thinner resulting in lower permeability rate. One of these changes (in polyamide and polysulfone) will be more restrictive and will act as limiting factor defining the final performance characteristic of the membrane. Being said that, systematic analyses are recommended to verify the current model and make sure that the contributions of each layer are reflected in the outcome of the performance simulation model.

Table 6.1. Individual changes of the polyamide and polysulfone layer that can contribute to the final performance of the compacted membrane

Layer	Status	Permeability	Salt Passage
Polyamide	High cross-linking rate	↓	↓
	Low cross-linking rate	↑	↑
	Neagatively charged	equal	↓
	Positively charged	depends*	↑
	Thinner layer	↑	↓
	Thicker layer	↓	↑
	High surface roughness	equal	equal
	Low surface roughnes	equal	equal
Polysulfone	High porosity rate	↑	↓
	Low porosity rate	↓	↑
	Thinner layer	↑	↓
	Thicker layer	↓	↑
	Asymmetric	equal	equal
	More asymmetric	↑	↓
	Symmetric surface	↓	↑
	Symmetric bulk	↑	↓

↑ increasing trend

↓ decreasing trend

* several factors may influence the final performance

6.3   Final remarks

The research done in the framework of this thesis offers new approaches and defines new areas towards fundamental understanding of the performance of reverse osmosis membranes. Advanced analytical techniques have been employed to tackle compaction phenomenon in seawater reverse osmosis membranes. Proof of concept based on pure theoretical assumption has been validated through expanding the boundaries of the existing understanding about the problem.

The work presented here may serve as inspiration and base for more systematic research that can lead to creation of novel membrane recipes, new product development and innovation.